

<https://helda.helsinki.fi>

Bridging Thermal Infrared Sensing and Physically-Based Evapotranspiration Modeling : From Theoretical Implementation to Validation Across an Aridity Gradient in Australian Ecosystems

Mallick, Kaniska

2018-05

Mallick , K , Toivonen , E , Trebs , I , Boegh , E , Cleverly , J , Eamus , D , Koivusalo , H ,
Drewry , D , Arndt , S K , Griebel , A , Beringer , J & Garcia , M 2018 , ' Bridging Thermal
Infrared Sensing and Physically-Based Evapotranspiration Modeling : From Theoretical
Implementation to Validation Across an Aridity Gradient in Australian Ecosystems ' , Water
Resources Research , vol. 54 , no. 5 , pp. 3409-3435 . <https://doi.org/10.1029/2017WR021357>

<http://hdl.handle.net/10138/298954>

<https://doi.org/10.1029/2017WR021357>

cc_by

publishedVersion

Downloaded from Helda, University of Helsinki institutional repository.

This is an electronic reprint of the original article.

This reprint may differ from the original in pagination and typographic detail.

Please cite the original version.



Water Resources Research

RESEARCH ARTICLE

10.1029/2017WR021357

Special Section:

Hydrology Delivers Earth System Sciences to Society (HESSS4): Improving and Integrating Knowledge Across Disciplines on Global Energy, Water and Carbon Cycles

Key Points:

- Thermal remote sensing of evapotranspiration is critical due to uncertainties in aerodynamic temperature and conductance estimation
- We integrated radiometric temperature into Penman-Monteith Shuttleworth-Wallace framework to directly estimate conductances and evapotranspiration
- Moderate to low systematic errors in evapotranspiration across an aridity gradient in Australia

Supporting Information:

- Supporting Information S1

Correspondence to:

K. Mallick,
kaniska.mallick@gmail.com;
E. Toivonen,
erika.a.toivonen@gmail.com

Citation:

Mallick, K., Toivonen, E., Trebs, I., Boegh, E., Cleverly, J., Eamus, D., et al. (2018). Bridging thermal infrared sensing and physically-based evapotranspiration modeling: From theoretical implementation to validation across an aridity gradient in Australian ecosystems. *Water Resources Research*, 54, 3409–3435. <https://doi.org/10.1029/2017WR021357>.

Received 21 JUN 2017

Accepted 9 APR 2018





Accepted article online 16 APR 2018

Published online 13 MAY 2018

© 2018. The Authors.

This is an open access article under the terms of the Creative Commons Attribution-NonCommercial-NoDerivs License, which permits use and distribution in any medium, provided the original work is properly cited, the use is non-commercial and no modifications or adaptations are made.

Bridging Thermal Infrared Sensing and Physically-Based Evapotranspiration Modeling: From Theoretical Implementation to Validation Across an Aridity Gradient in Australian Ecosystems

Kaniska Mallick¹ , Erika Toivonen^{1,2,3,4} , Ivonne Trebs¹, Eva Boegh^{5,6}, James Cleverly⁷ , Derek Eamus⁷ , Harri Koivusalo², Darren Drewry^{8,9}, Stefan K. Arndt¹⁰, Anne Griebel¹⁰, Jason Beringer¹¹ , and Monica Garcia^{12,13}

¹Department of Environmental Research and Innovation, Luxembourg Institute of Science and Technology, Belvaux, Luxembourg, ²Department of Built Environment, Aalto University School of Engineering, Espoo, Finland, ³Climate System Research, Finnish Meteorological Institute, Helsinki, Finland, ⁴Department of Physics, University of Helsinki, Helsinki, Finland, ⁵Department of Science and Environment, Roskilde University, Roskilde, Denmark, ⁶Now at Danish Agency for Data Supply and Efficiency, Copenhagen, Denmark, ⁷Terrestrial Ecohydrology Research Group, School of Life Sciences, University of Technology Sydney, Broadway, NSW, Australia, ⁸Jet Propulsion Laboratory, California Institute of Technology, Pasadena, CA, USA, ⁹Joint Institute for Regional Earth System Science and Engineering, University of California, Los Angeles, CA, USA, ¹⁰School of Ecosystem and Forest Sciences, University of Melbourne, Melbourne, Vic, Australia, ¹¹School of Agriculture and Environment, University of Western Australia, Crawley, WA, Australia, ¹²Department of Environmental Engineering, Technical University of Denmark, Kgs. Lyngby, Denmark, ¹³International Research Institute for Climate and Society, Earth Institute, Columbia University, Palisades, NY, USA

Abstract Thermal infrared sensing of evapotranspiration (E) through surface energy balance (SEB) models is challenging due to uncertainties in determining the aerodynamic conductance (g_A) and due to inequalities between radiometric (T_R) and aerodynamic temperatures (T_0). We evaluated a novel analytical model, the Surface Temperature Initiated Closure (STIC1.2), that physically integrates T_R observations into a combined Penman-Monteith Shuttleworth-Wallace (PM-SW) framework for directly estimating E , and overcoming the uncertainties associated with T_0 and g_A determination. An evaluation of STIC1.2 against high temporal frequency SEB flux measurements across an aridity gradient in Australia revealed a systematic error of 10–52% in E from mesic to arid ecosystem, and low systematic error in sensible heat fluxes (H) (12–25%) in all ecosystems. Uncertainty in T_R versus moisture availability relationship, stationarity assumption in surface emissivity, and SEB closure corrections in E were predominantly responsible for systematic E errors in arid and semi-arid ecosystems. A discrete correlation (r) of the model errors with observed soil moisture variance ($r = 0.33$ – 0.43), evaporative index ($r = 0.77$ – 0.90), and climatological dryness ($r = 0.60$ – 0.77) explained a strong association between ecohydrological extremes and T_R in determining the error structure of STIC1.2 predicted fluxes. Being independent of any leaf-scale biophysical parameterization, the model might be an important value addition in working group (WG2) of the Australian Energy and Water Exchange (OzEWEX) research initiative which focuses on observations to evaluate and compare biophysical models of energy and water cycle components.

Plain Language Summary Evapotranspiration modeling and mapping in arid and semi-arid ecosystems are uncertain due to empirical approximation of surface and atmospheric conductances. Here we demonstrate the performance of a fully analytical model which is independent of any leaf-scale empirical parameterization of the conductances and can be potentially used for continental scale mapping of ecosystem water use as well as water stress using thermal remote sensing satellite data.

1. Introduction

The determination of the aerodynamic temperature (T_0) and conductance (g_A) contributes to the principal uncertainty in regional-scale evapotranspiration (E) mapping when using models based on thermal infrared

sensing (Kustas et al., 2016; Paul et al., 2014, 2013). To reduce this uncertainty, there is either a sincere need to accommodate and settle on a unified land surface parameterization for estimating T_0 and g_A ; or use analytical models independent of any empirical parameterization of these variables.

Land surface temperature or radiometric surface temperature (T_R) obtained through thermal infrared remote sensing governs the land surface energy budget (Anderson et al., 2012; Kustas & Anderson, 2009), and thermal E models principally focus on surface energy balance (SEB) approach in which T_R represents the lower boundary condition to constrain the energy-water fluxes (Anderson et al., 2008; Mallick et al., 2014a, 2015; Norman et al., 1995). It satisfies the SEB equation (equations (1)–(3)) by altering T_0 as well as by imposing constraints arising due to water stress on the biophysical conductances (g_A and g_C) (a list of variables and symbols along with their units are given in Table A1).

$$R_N = H + \lambda E + G \quad (1)$$

$$(R_{S\downarrow} - R_{S\uparrow}) + (R_{L\downarrow} - \rho \epsilon T_R^4) = \rho C_P g_A (T_0 - T_A) + \frac{\rho C_P g_A g_C}{\gamma(g_A + g_C)} (e_0^* - e_A) + G \quad (2)$$

$$T_R = \left[\frac{(R_{S\downarrow} - R_{S\uparrow}) + R_{L\downarrow} - \rho C_P g_A (T_0 - T_A) - \frac{\rho C_P g_A g_C}{\gamma(g_A + g_C)} (e_0^* - e_A) - G}{\rho \epsilon} \right]^{\frac{1}{4}} \quad (3)$$

State-of-the-art SEB models are based on estimating g_A and sensible heat flux (H) while solving E (or latent heat flux, λE) as a residual SEB component (given R_N and G are known). However, the most serious assumption in estimating H concerns the use of T_R as a surrogate of T_0 (Chávez et al., 2010; Colaizzi et al., 2004). Major drawbacks in the explicit use of T_R in SEB modeling are (a) the inequality between T_0 and T_R ($T_0 \neq T_R$) (Boulet et al., 2015; Chávez et al., 2010), (b) the unavailability of a universally agreed model to estimate T_0 , which controls the transfer of sensible heat (Colaizzi et al., 2004), (c) nonunique relationship between T_0 and T_R due to differences between the effective source-sink height of momentum and heat within vegetation substrate complex (Chávez et al., 2010; Holwerda et al., 2012; Troufleur et al., 1997), (d) the lack of a preeminent physically-based g_A model (Holwerda et al., 2012), and (e) bypassing the role of T_R on g_C in λE modeling.

Despite the aforementioned shortcomings, emphasis on estimating H is motivated by the broad acceptance of the Monin-Obukhov Similarity Theory (MOST) or Richardson Number (R_i) criteria for estimating g_A , and the requirement of minimum inputs for solving both g_A and H . However, estimating g_A using MOST or R_i approaches created further problems, particularly in relation to accommodating the inequalities between T_0 and T_R , as well as in adapting the differences between g_A and the momentum conductance (g_M) arising due to the differences in the roughness length of heat and momentum (z_{OH} and z_{OM}) (Paul et al., 2014). The effects due to inequality between T_0 and T_R were partially overcome by the inclusion of an “extra conductance” and the kB^{-1} term as a fitting parameter that adjusts the difference between z_{OH} and z_{OM} (Boegh et al., 2002; Su, 2002; Troufleur et al., 1997), and later through the inception of two-source soil-canopy modeling schemes (Anderson et al., 2007; Boulet et al., 2015; Colaizzi et al., 2012; Norman et al., 1995). However, SEB-based predictions of H (and λE) are conditional to empirical response functions of g_A (Ershadi et al., 2015; Kustas et al., 2016; Liu et al., 2007; Morillas et al., 2013; Paul et al., 2014; Timmermans et al., 2013) that have an uncertain transferability in space and time (Holwerda et al., 2012; van Dijk et al., 2015). In contemporary SEB modeling, g_A submodels are stand-alone, and lack the necessary physical feedback it should provide to g_C , T_0 , and vapor pressure deficit surrounding the evaporating surface (D_0) (Cleverly et al., 2013). The feedback of g_A on g_C is critical in arid and semi-arid ecosystems where reduced soil moisture availability in conjunction with very high evaporative potential causes significant water stress in the soil-vegetation-atmosphere system, thereby resulting discrepancy between T_R and T_0 . Thermal-based λE modeling needs explicit consideration of such important biophysical feedbacks to reduce the existing uncertainties in arid and semi-arid ecosystems (Kustas et al., 2016).

The Penman-Monteith (PM) and Shuttleworth-Wallace (SW) models are mutually related and two of the most preeminent physical models for quantifying surface-to-air λE . They are fundamentally constrained to account for the necessary feedbacks between λE , T_R , D_0 , g_A , and g_C (Monteith, 1965; Shuttleworth & Wallace, 1985). The elemental connectivity of PM-SW with T_R originates from the first-order dependence of g_C and g_A on T_R (through soil moisture and T_0). Despite their theoretical integrity, the integration of T_R into the PM-

SW model was not yet well established. Although the perception of combining the PM model with T_R was initiated by Jackson et al. (1981) in the Crop Water Stress Index (CWSI) formulation, it had later been acknowledged that using the PM method could produce large errors in λE due to the underlying uncertainties in conductance estimates, particularly in sparsely vegetated and water-stressed ecosystems (Leuning et al., 2008; Morillas et al., 2013), such as the majority of ecosystems in Australia (Beringer et al., 2016).

Invigorated by the potential of thermal infrared data, Mallick et al. (2014a, 2015) proposed an integration of T_R into the PM model to directly estimate the conductances, λE , and H , and to simultaneously overcome the empirical uncertainties in estimating g_A and T_0 . The Surface Temperature Initiated Closure (STIC) (Mallick et al., 2014a, 2015) is a unique framework based on analytical solutions for g_A , g_C , and T_0 . Initial studies with different versions of STIC primarily focused on validation of H , λE , and its partitioning, using moderate (coarse) spatial (temporal) resolution remote sensing data (STIC1.0; Mallick et al., 2014a), and understanding the impacts of thermal versus humidity based water stress constraints on λE (STIC1.1; Mallick et al., 2015). However, the early versions of STIC could only partially bridge T_R and SEB modeling due to structural inadequacies for establishing surface versus aerodynamic feedbacks (Mallick et al., 2015). A later version of STIC (STIC1.2) (Mallick et al., 2016) integrates T_R into the PM-SW system to establish the required feedback between T_R and λE , along with aerodynamic temperature, humidity, and conductances. In a recent study, STIC1.2 was applied for evaluation of biophysical conductances and assessing their controls on evapotranspiration partitioning in the Amazon basin (Mallick et al., 2016). However, evaluating the performance of STIC1.2 across an aridity gradient with data of high temporal resolution is on one hand essential to understand the role of T_R in STIC1.2 in hydrologically extreme natural ecosystems, and on the other to evaluate the limitations of this analytical SEB model before extending its future applicability for regional-scale E mapping.

The combination of prevailing arid/semi-arid ecosystems, ecohydrological heterogeneity, and the availability of continuous SEB flux observations make Australia an excellent test bed. Present study reports an in-depth evaluation of STIC1.2 by exploring eddy covariance (EC) observations from a range of diverse ecosystems of the OzFlux network (Beringer et al., 2016) across a large aridity gradient in Australia as a way forward to reduce T_0 and g_A uncertainties in regional-scale E mapping as well as to efficiently bridge T_R and SEB modeling. Our study addressed the following research questions:

1. What is the performance of STIC1.2 when evaluated with high temporal resolution data across an aridity gradient in Australia?
2. How do T_R and environmental variables affect the performance of STIC1.2 across ecohydrological extremes from arid to mesic ecosystems?
3. Is there an association between ecohydrological conditions and T_R in determining the errors and variability of water and energy flux components predicted by STIC1.2?

The novelties of the present study are: (a) an extensive evaluation of STIC1.2 from dry to wet ecohydrological extremes at multiple temporal scales (from half-hourly to annual), (b) intercomparison with previous versions of STIC, (c) analyzing the sensitivity of λE and conductances to T_R , as well as application of multivariate statistics (e.g., principal component analysis) to understand the impacts of T_R and environmental variables on the error characteristics of STIC1.2 derived λE from arid to mesic climate, and (d) identification of the integrated role of ecohydrological conditions and T_R on errors and variability of SEB flux predictions by STIC1.2.

2. Why Australia?

Australia is a predominantly dry continent with substantial fluctuations in precipitation and primary production (Cleverly et al., 2016). Limited water resources, drought vulnerability, high evaporative demand, and growing water requirements are continuously increasing pressure on sustainable management of water resources. The Millennium Drought from 2001 to 2009 dramatically ended with a “big wet” in 2010–2012 coinciding with the largest La Niña in over 70 years (Cleverly et al., 2016; van Dijk et al., 2013). A major part of the Australian continent is arid (38%) or semi-arid (36%) (Beringer et al., 2016) with canopy cover of less than 50% across most of the continent (Glenn et al., 2011). In contrast, there are locations where annual average precipitation exceeds 4,000 mm (Glenn et al., 2011). In most areas of the continent, potential evaporation (E_p) exceeds precipitation (P), and approximately 90% of P returns back to the atmosphere as E

(Glenn et al., 2011) with the residue generating surface and groundwater resources (Guerschman et al., 2009). Strong land-atmosphere coupling in these regions makes the estimation of SEB fluxes very sensitive to the boundary conditions and underlying assumptions of biophysical parameterization, a situation that is often confounded by extreme heterogeneity in evaporation versus transpiration and their contrasting responses to surface soil water content. Hence, observation, monitoring, and prediction of water and energy flux components are imperative in these regions to meet the challenge of developing and implementing sustainable water resource management decisions (Martens et al., 2016). Therefore, detailed evaluation of a physically-based SEB model like STIC1.2 is the prerequisite before applying it for a reliable prediction and management of water resources in Australia and globally.

3. Methodology

3.1. Theory

STIC (version STIC1.2) is a one-dimensional SEB model that treats soil-vegetation as a single unit (Figure 1). The fundamental assumption in STIC is the first-order dependence of g_A and g_C on aerodynamic temperature (T_0) and soil moisture (θ) through T_R , which allows direct integration of T_R into the PM-SW system (Mallick et al., 2016). The integration of T_R into PM-SW system is done by first estimating aggregated surface moisture availability (M) as a function of T_R , followed by simultaneously constraining the two biophysical conductances through M in an analytical framework. STIC1.2 exploits radiation (net radiation (R_N), ground heat flux (G)) and meteorological variables (air temperature (T_A), relative humidity (R_H) or vapor pressure (e_A)) at the reference level) in conjunction with T_R observations as external inputs.

The expressions of λE and H according to the PM equation are as follows (Monteith, 1965):

$$\lambda E = \frac{s\phi + \rho c_p g_A D_A}{s + \gamma \left(1 + \frac{g_A}{g_C}\right)} \quad (4a)$$

$$H = \frac{\gamma \phi \left(1 + \frac{g_A}{g_C}\right) - \rho c_p g_A D_A}{s + \gamma \left(1 + \frac{g_A}{g_C}\right)} \quad (4b)$$

For a full vegetation and (or) bare surface, g_C represents the canopy conductance and (or) bare surface conductance, respectively. In the case of partial canopy cover, g_C represents an aggregated surface conductance of both canopy and soil. The effects of this simplified representation of aggregated g_C on the performance of STIC1.2 is represented in Figures 9b, 9d, and 9f) which shows the residual λE error (modeled minus observed λE) versus g_C for different vegetation types.

The two unknown “state variables” in equations (4a) and (4b) are g_A and g_C , and the main goal of STIC1.2 is to find an analytical solution of the two unobserved conductances from measurements of radiative, meteorological, and radiometric conditions (Mallick et al., 2014a, 2015, 2016). This will simultaneously find a “closure” of the PM model. As neither g_A nor g_C can be measured at the canopy-scale or at large spatial scales (van Dijk et al., 2015), a “closure” of the PM equation is only possible through an analytical estimation of the conductances. Consequently, multiple “state equations” were formulated to obtain closed-form expressions of g_A and g_C . In the state equations, a direct connection of T_R (through M) is initiated in the expression of evaporative fraction (Λ), which is simultaneously propagated into equations of g_A , g_C , and T_0 (equations (5)–(8)).

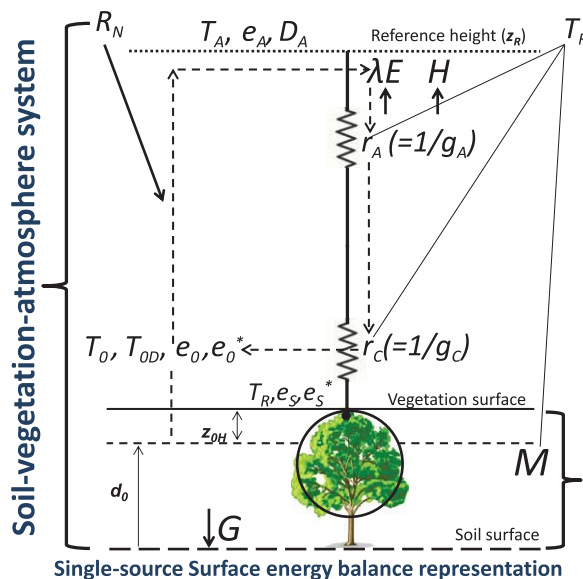


Figure 1. Schematic representation of one-dimensional description of STIC1.2. In STIC1.2, a feedback is established between the surface layer evaporative fluxes and source/sink height mixing and coupling, and the connection is shown in dotted arrows between e_0 , e_0^* , g_A , g_C , and λE . Here r_A and r_C are the aerodynamic and canopy (or canopy-substrate complex in case of partial vegetation cover) resistances, g_A and g_C are the aerodynamic and canopy conductances (reciprocal of resistances), e_s^* is the saturation vapor pressure at the surface, e_0^* is the saturation vapor pressure at the source/sink height, T_0 is the source/sink height temperature (i.e., aerodynamic temperature) that is responsible for transferring the sensible heat (H), e_0 is the source/sink height vapor pressure, e_s is the vapor pressure at the surface, z_{0H} is the roughness length for heat transfer, d_0 is the displacement height, T_R is the radiometric surface temperature, T_{OD} is the source/sink height dewpoint temperature, M is the surface moisture availability or evaporation coefficient, R_N and G are net radiation and ground heat flux, T_A , e_A , and D_A are temperature, vapor pressure, and vapor pressure deficit at the reference height (z_R), λE is the latent heat flux, respectively.

$$\Lambda = \frac{2\alpha s}{2s + 2\gamma + \gamma \frac{g_A}{g_C} (1+M)} \quad (5)$$

$$T_0 = T_A + \left(\frac{e_0 - e_A}{\gamma} \right) \left(\frac{1 - \Lambda}{\Lambda} \right) \quad (6)$$

$$g_A = \frac{\phi}{\rho C_P \left[(T_0 - T_A) + \left(\frac{e_0 - e_A}{\gamma} \right) \right]} \quad (7)$$

$$g_C = g_A \frac{(e_0 - e_A)}{(e_0^* - e_0)} \quad (8)$$

The functional forms of equations (5)–(8) and their detailed derivations are given in the supporting information and in Mallick et al. (2014a, 2015, 2016). Given values of M , R_N , G , T_A , and R_H or e_A , the four state equations (equations (5)–(8)) can be solved simultaneously to derive analytical solutions for the four unobserved state variables. However, the analytical solutions to the four state equations have three accompanying unknowns; e_0 (vapor pressure at the source/sink height), e_0^* (saturation vapor pressure at the source/sink height), and Priestley-Taylor coefficient (α) (Priestley & Taylor, 1972), and as a result there are four equations with seven unknowns. Consequently, an iterative solution must be found to determine the three unknown variables (as described in supporting information) (also in Mallick et al., 2016). For estimating source/sink height vapor pressures we applied equation (8) from Shuttleworth and Wallace (1985), and thus STIC1.2 uniquely combines both the Penman-Monteith and Shuttleworth-Wallace (PM-SW) models (described in supporting information) (also Mallick et al., 2016). In equation (8), the Priestley-Taylor coefficient (α) appeared due to using the Advection-Aridity (AA) hypothesis (Brutsaert & Stricker, 1979) for deriving the state equation of Λ (Mallick et al., 2016, 2015) (details in supporting information). However, instead of optimizing α as a “fixed parameter,” α is dynamically estimated by constraining it as a function of M , conductances, aerodynamic vapor pressure, and temperature (Mallick et al., 2016). The derivation of the equation for α is described in supporting information.

STIC1.2 consists of a feedback loop describing the relationship between T_R and λE , coupled with canopy-atmosphere components relating λE to T_0 and e_0 (Mallick et al., 2016). For estimating M , T_R is extensively used in a physical retrieval framework (detailed in SI) (also in Mallick et al., 2016), which allows an integration of T_R into a physically-based SEB model. Upon finding analytical solution of g_A and g_C , both the variables are returned into equations (4a) and (4b) to directly estimate λE and H .

3.2. Estimation of T_R

Estimation of T_R was based on the observed upwelling longwave radiation ($R_{L\uparrow}$) and the Stefan-Boltzmann equation $\left[T_R = \left(\frac{R_{L\uparrow}}{\delta \varepsilon} \right)^{0.25} \right]$ (Formetta et al., 2016; Park et al., 2008; Sun & Pinker, 2003) (ε is the infrared surface emissivity, δ is the Stefan-Boltzmann constant). Upwelling longwave radiation was directly measured with pyrgeometer in all the study sites. The Advanced Spaceborne Thermal Emission and Reflection Radiometer (ASTER) Global Emissivity Dataset (GED) land surface emissivity data product (Göttsche & Hulley, 2012; Hulley et al., 2015) (product name: AG100V003; spatial resolution: 100 m, temporal frequency: static) (https://lpdaac.usgs.gov/dataset_discovery/community/community_products_table) was used in the inverted Stefan-Boltzmann equation for estimating T_R . This ε database is developed by the National Aeronautics and Space Administration's (NASA) Jet Propulsion Laboratory (JPL), California Institute of Technology, and ASTER data from 2000 to 2008 are used to generate this infrared emissivity record. For every site, the corresponding ε is given in Table 1.

3.3. SEB Closure

The statistical intercomparisons of STIC1.2 results against SEB flux observations were performed by forcing energy balance closure by adding energy to λE and H in proportion to the measured Bowen ratio ($H/\lambda E$; BREB-closure) (Bowen, 1926) as described by Chávez et al. (2005) and later adopted by Anderson et al. (2008) and Mallick et al. (2014a, 2015, 2016). However, in order to understand the effects of SEB closure correction methods on the statistical error metric, residual SEB closure correction (RES-closure) was also tested in which actual λE observations were neglected (Majozi et al., 2017), and λE was estimated as a residual of

Table 1
An Overview of Sites, Their Aridity Index (AI) Class and Characteristics (Numbers in the Parentheses Represent the Coefficient of Variation)

Aridity index (AI) class	Site name	OzFlux ID	Region	Latitude (S) Longitude (E)	World ecoregion	Land cover	AI	Annual T _A (°C)	Annual		Annual E/R _N	EBC		Data availability λE & H (%)
									P (mm yr ^{−1})	E (mm yr ^{−1})		ε	%	
Arid (0 < AI < 0.2)	Alice Springs	AU-ASM	Northern Territory	−22.28° 133.25°	Deserts and Xeric shrublands	Semi-arid mulga (Acacia aneura) ecosystem	0.04–0.11	(−4) to 46	306 (58)	141 (100)	0.10	0.800	60–61	95
	Calperum	AU-Cpr	South Australia	−34.00° 140.59°	Mediterranean woodlands	Recovering mallee woodland	0.05–0.06	12–45	240 (60)	257 (77)	0.13	0.800	72–78	79
	Great Western Woodlands	AU-GWW	Western Australia	−30.19° 120.65°	Mediterranean woodlands	Temperate woodland, shrubland and mallee	0.05–0.14	5–33	240 (41)	135 (77)	0.17	0.810	56–58	85
	Ti Tree East	AU-TTE	Northern Territory	−22.29° 133.64°	Deserts and Xeric shrublands	Grassy mulga woodland and Corymbia/Triodia savanna	0.05–0.11	(−4) to 46	305 (80)	144 (100)	0.11	0.835	72–75	86
Semi-arid (0.2 < AI < 0.5)	Gingin	AU-Gin	Western Australia	−31.38° 115.71°	Mediterranean woodlands	Coastal heath Banksia woodland	0.20–0.26	19–30	641 (19)	486 (63)	0.29	0.805	77–78	84
	Jaxa (Yanco)	AU-Ync	New South Wales	−34.99° 146.29°	Temperate grassland	Grassland	0.30–0.41	12–37	465 (34)	207 (100)	0.10	0.800	57–76	86
	Riggs Creek	AU-Rig	Victoria	−36.65° 145.58°	Pasture	Dryland agriculture	0.45–0.46	12–26	650 (23)	297 (84)	0.30	0.910	80–81	70
	Sturt Plains	AU-Stp	Northern Territory	−17.15° 133.35°	Tropical grassland	Low lying plain dominated by Mitchell Grass	0.22–0.33	11–39	640 (37)	454 (100)	0.28	0.880	82–93	90
Mesic (0.5 < AI)	Whroo	AU-Whr	Victoria	−36.67° 145.03°	Temperate woodlands	Box woodland	0.20–0.22	3–30	558 (52)	443 (62)	0.27	0.810	93–95	90
	Wombat	AU-Wom	Victoria	−37.42° 144.09°	Temperate broadleaf forest	Dry sclerophyll eucalypt forest	0.23–0.39	1–30	650 (10)	653 (62)	0.43	0.925	71–73	87
	Cowbay	AU-Cow	Queensland	−16.24° 144.09°	Tropical and subtropical moist broadleaf forests	Complex mesophyll vine forest	2.30–2.90	11–39	4,000 (10)	745 (55)	0.61	0.955	89–91	88
	Cumberland Plains	AU-Cum	New South Wales	−33.62° 150.72°	Temperate woodlands	Dry sclerophyll	0.56–0.76	3–29	800 (24)	486 (66)	0.43	0.885	81–91	85
	Dry River	AU-Dry	Northern Territory	−15.26° 132.37°	Tropical savannas	Open forest savanna	0.50–0.73	14–37	895 (36)	679 (73)	0.47	0.970	80–81	92
	Howard Springs	AU-How	Northern Territory	−12.49° 131.15°	Tropical savannas	Tropical savanna (wet)	0.53–0.64	20–33	1,700 (25)	1,190 (60)	0.56	0.870	85–91	96
	Tumbarumba	AU-Tum	New South Wales	−35.66° 148.15°	Temperate broadleaf and mixed forest	Wet temperate sclerophyll eucalypt	0.65–0.77	(−10) to 30	1,000 (15)	955 (90)	0.68	0.970	72–75	89

R_N , G , and H . Caution in using RES-closure method has been previously given by Barr et al. (2012) because it is very unlikely that measurements of R_N , G or H are without error.

4. Data Sets and Statistical Analysis

4.1. Eddy Covariance and Meteorological Quantities

In the present analysis, we have used data from the regional Australian and New Zealand EC flux tower network, OzFlux (<http://data.ozflux.org.au/portal/pub/listPubCollections.jsp>). OzFlux EC stations are distributed among ecohydrologically contrasting landscapes in Australia and New Zealand to provide national data of energy, water, and carbon fluxes at a continental scale to improve our understanding of the responses of these surface-atmosphere fluxes of Australian ecosystems to current climate as well as future climate change (Beringer et al., 2016).

We explored the level-3 quality controlled and harmonized surface flux and meteorological data for the years 2013 and 2014 from 15 (out of 26) active Australian OzFlux sites located across nine different ecoregions in Australia (Figure 2 and Table 1): deserts and xeric shrublands (AU-ASM, AU-TTE), pasture (AU-Rig), Mediterranean woodlands (AU-Cpr, AU-Gin, AU-GWW), temperate broadleaf (and mixed) forest (AU-Tum, AU-Wom), temperate grassland (AU-Ync), temperate woodlands (AU-Cum, AU-Whr), tropical and subtropical moist broadleaf forest (AU-Cow), tropical grassland (AU-Stp), and tropical savannas (AU-How, AU-Dry). We divided these sites into three broad aridity classes based on their aridity index (AI) (ratio of annual P and E_p ; i.e., P/E_p): arid ($0 < AI < 0.2$, AU-ASM, AU-Cpr, AU-GWW, and AU-TTE); semi-arid ($0.2 < AI < 0.5$, AU-Gin, AU-Rig, AU-Stp, AU-Whr, AU-Wom, and AU-Ync); and mesic (subhumid and humid) ($0.5 < AI$, AU-Cow, AU-Cum, AU-Dry, AU-How, and AU-Tum) (<http://www.bom.gov.au>). In Table 1, annual values of P and T_A are the climatological averages of every site which are reported in <http://www.ozflux.org.au/monitoringsites/>. Annual E and R_N were computed from the available EC tower data sets for 2013 and 2014. Annual E_p was computed from FAO (Food and Agricultural Organisation) Penman-Monteith equation (Allen et al., 1998).

The main reason for selecting 2013 and 2014 was the rainfall deficit which followed the anomalously wet period of 2010 and 2011 in Australia (Cleverly et al., 2016; Ma et al., 2016) and continued to worsen to severe drought through 2014 across the continent (<http://www.bom.gov.au/climate/drought/archive/>). According to these criteria, data availability in these 2 years coincided for the selected 15 sites.

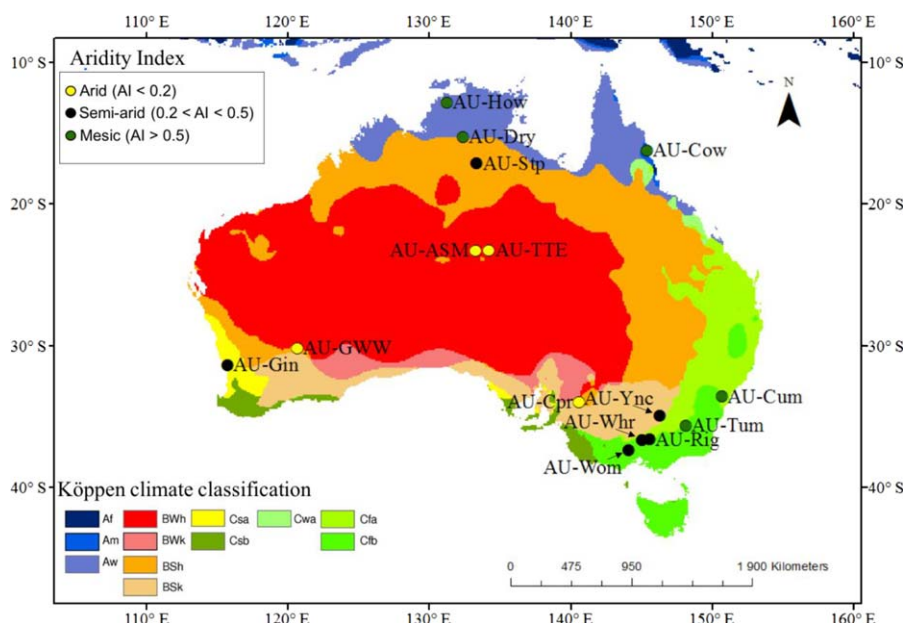


Figure 2. Climatic map of Australia with the distribution of 15 eddy covariance sites (source of the base map: <http://people.eng.unimelb.edu.au/mpeel/Koppen/Australia.jpg>).

The data are available at half-hourly temporal resolution, with an exception at AU-Tum where the temporal resolution of the data is 1 h. Data used for this analysis included time series of surface energy balance fluxes (R_N , λE , H , G), shortwave and longwave radiation components ($R_{S\downarrow}$, $R_{S\uparrow}$, $R_{L\downarrow}$, $R_{L\uparrow}$), and hydrometeorological variables (e.g., T_A , R_H , u , u^* , θ , and P). A general description of the site characteristics can be found in Table 1 and also in Beringer et al. (2016). Daily SEB fluxes (in W m^{-2}) were computed by averaging half-hourly (hourly for AU-Tum) observed fluxes and those predicted by STIC1.2. Monthly and annual E (in mm) and H (converted to water equivalent in mm) (<http://www.fao.org/docrep/x0490e/x0490e07.htm>) were computed by summing daily λE and H values. We did not perform any gap filling, which implies that missing observed or estimated subdaily or daily λE and H values (for data availability see Table 1) were not included in the computation.

Performance of STIC 1.2 was also evaluated for dry and wet seasons (Appendix A2), whereby the seasons were defined based on monthly P and θ . The timing and duration of the seasons varied between different sites. A table of dry and wet seasons for the individual sites are given in Table A3.

4.2. Statistical Analysis

4.2.1. Multitemporal SEB Flux Assessment

In order to evaluate the performance of STIC1.2, we used different statistical metrics: root-mean-square deviation (RMSD), relative root-mean-square deviation (RRMSD), the coefficient of determination (R^2), mean absolute percentage deviation (MAPD), and the ratio of squared systematic RMSD to squared RMSD ($\text{RMSD}_s^2/\text{RMSD}^2$) (equations (A1)–(A4) in Appendix). Predicted λE and H were compared with observed values for each study site at sub-daily, daily, and annual scales. Results and discussions on multitemporal SEB flux estimation statistics are given in sections 5.1 and 6.1, respectively.

4.2.2. Assessing the Role of T_R and Associated Environmental Variables on the Performance of STIC1.2

A sensitivity analysis and a Principal Component Regression (PCR) analysis (Jolliffe, 2002) were performed to assess the impact of T_R and environmental variables on the relative change in λE error (in percent) and residual error of λE (i.e., $\Delta_{\lambda E}$ = difference between λE predicted by STIC1.2 and observed λE). Sensitivity of λE to T_R was tested by introducing random uncertainty in the surface emissivity to generate uncertain T_R scenarios at half-hourly time steps. The relative change in λE error due to the relative change in T_R was estimated for every time step and correlation between them was evaluated for different classes of θ and E_p/ϕ ratios. PCR was performed on a correlation matrix of five variables which are: T_R , D_A , ϕ , wind speed (u), and $\Delta_{\lambda E}$. The correlation between $\Delta_{\lambda E}$ and principal component (PC) is known as "loading." Loadings close to ± 1 indicate that the variable has substantial impact on $\Delta_{\lambda E}$. PCs with high loadings generally explain maximum variances in $\Delta_{\lambda E}$ and are considered in evaluating the impacts on $\Delta_{\lambda E}$. Results of the sensitivity analysis and PCR are presented in section 5.2 with extended discussions in section 6.2.

4.2.3. Relationship Between Ecohydrological Factors and T_R in Determining the Errors and Variability of SEB Fluxes Predicted by STIC1.2

To examine the link between ecohydrological conditions and T_R on the SEB flux predictions, we further investigated the patterns of MAPD in daily λE and H in comparison to the coefficient of variation of observed soil moisture (cV_θ), annual evaporative index (i.e., annual E/R_N), climatic dryness (i.e., annual E_p/P) (Donohue et al., 2010), and emissivity (ε), which are considered to represent the ecohydrological characteristics of ecosystems that are intrinsically related to T_R . Arid and semi-arid ecosystems generally have large variations in ε (Hulley et al., 2010; Masiello et al., 2014) which is mostly associated with high cV_θ , low E/R_N , and high E_p/P (high evaporative demand and low precipitation). Therefore, assessing the effects of a single value of ε on the predictive capacity of STIC1.2 is crucial. Results of the correlation analysis between MAPD of daily λE (and H) with ε , annual cV_θ , annual E/R_N , and annual E_p/P of each site is presented in section 5.3 and discussions are elaborated in section 6.3.

5. Results

5.1. Performance of STIC1.2 Across an Aridity Gradient in Australia

The box-plots of statistical errors of half-hourly λE for three ecohydrologically contrasting ecosystem classes revealed STIC1.2 to explain 60–85% of the observed λE variability (R^2 0.60–0.85), with mean MAPD of 30–50%, and mean RMSD 36–55 W m^{-2} in the mesic and semi-arid sites (Figures 3a, 3c, and 3e, please see Table 2 for site statistics). For the arid sites, STIC1.2 explained 40% of the observed λE variability, with RMSD

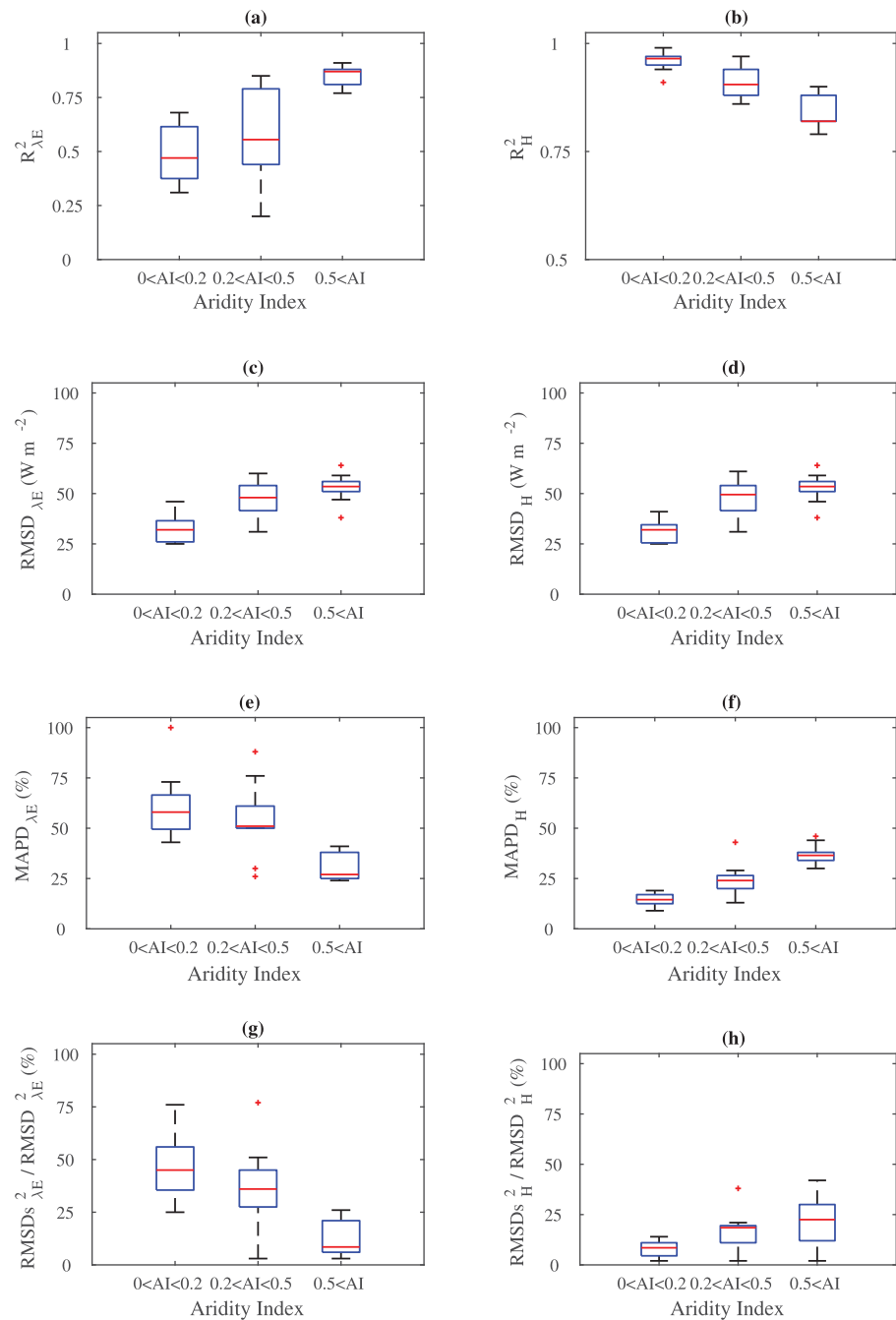


Figure 3. (a) Boxplots and whiskers of R^2 , (b) MAPD, (c) RMSD, and (d) $RMSD^2_{\lambda E} / RMSD^2_H$ between λE and H predicted by STIC1.2 versus observations in OzFlux ecosystems of contrasting aridity. The lower and upper bound of the box and the red line inside represents the first and third quartiles, and median values. The lower and upper whiskers represent minimum and maximum values of the statistics and the red line in the boxplot represent the mean values of the statistical metrics.

of $26\text{--}46\text{ W m}^{-2}$ (average 36 W m^{-2}) (78% of the observed mean) and relatively high MAPD (60%) (Figures 3a, 3c, and 3e). The average ratio of $RMSD^2_{\lambda E} / RMSD^2_H$ (i.e., systematic RMSD, %) was moderate to low in Semi-arid (35%, range 24–48%) and mesic (10%, range 3–23%) ecosystems (Figure 3g), which increased to 45% (range 30–60%) in the arid ecosystems, thus revealing high systematic λE error (along with high percent RMSD) in the water-limited ecosystems as compared to the radiation-limited ecosystems (Figure 3g). The predictive accuracy of H followed the opposite pattern compared to λE , featuring maximum R^2 (0.85–

Table 2

Error Statistics of Sub-daily λE and H Derived With STIC1.2 on 15 EC Sites Covering Three Ecohydrologically Contrasting OzFlux Ecosystems of Different Aridity Classes as Defined in Table 1

Aridity class	Site name	Year	λE				H			
			RMSD (W m^{-2})	R^2	MAPD (%)	$\text{RMSD}_s^2 / \text{RMSD}^2$ (%)	RMSD (W m^{-2})	R^2	MAPD (%)	$\text{RMSD}_s^2 / \text{RMSD}^2$ (%)
Arid ($0 < \text{AI} < 0.2$)	AU-ASM	2013	26	0.31	73	25	25	0.99	9	2
		2014	39	0.63	52	52	35	0.97	14	14
	AU-Cpr	2013	30	0.39	58	34	30	0.97	15	11
		2014	25	0.36	58	37	25	0.96	14	6
	AU-GWW	2013	34	0.54	47	60	34	0.94	19	7
		2014	34	0.60	43	42	34	0.96	15	11
Semi-arid ($0.2 < \text{AI} < 0.5$)	AU-TTE	2013	26	0.40	100	48	26	0.97	11	10
		2014	46	0.68	60	76	41	0.91	19	3
	AU-Gin	2013	53	0.55	50	34	53	0.90	25	17
		2014	54	0.54	54	24	54	0.91	24	20
	AU-Ync	2013	39	0.27	65	77	39	0.94	16	2
		2014	31	0.20	88	45	31	0.97	13	3
	AU-Rig	2013	60	0.48	57	51	61	0.86	29	21
		2014	59	0.40	76	45	60	0.87	43	38
	AU-Stp	2013	44	0.76	51	38	44	0.88	24	13
		2014	50	0.82	51	42	52	0.88	25	9
	AU-Whr	2013	43	0.56	51	21	43	0.94	21	18
		2014	46	0.58	50	32	47	0.94	21	19
Mesic ($0.5 < \text{AI}$)	AU-Wom	2013	40	0.85	26	3	40	0.95	19	19
		2014	54	0.82	30	31	54	0.89	28	19
	AU-Cow	2013	38	0.91	24	9	38	0.82	46	23
		2014	47	0.85	31	5	46	0.82	44	40
	AU-Cum	2013	51	0.81	41	25	51	0.89	36	14
		2014	52	0.77	40	8	52	0.90	31	22
	AU-Dry	2013	54	0.88	25	21	54	0.80	34	12
		2014	64	0.80	38	26	64	0.82	30	30
	AU-How	2013	55	0.89	24	7	55	0.82	38	42
		2014	59	0.87	26	16	59	0.79	38	25
	AU-Tum	2013	56	0.87	27	6	56	0.87	37	2
		2014	53	0.88	27	3	53	0.88	35	2

0.95) and minimum errors (10–25% MAPD and 35–50 W m^{-2} RMSD) in the water-limited ecosystems as compared to the wet ecosystems with R^2 of 0.80, MAPD 37%, and RMSD 55 W m^{-2} , respectively (Figures 3b, 3d, and 3f). Interestingly, the average ratio of $\text{RMSD}_s^2 / \text{RMSD}^2$ varied between 10% and 25% (Figure 3h), thus revealing low systematic errors in H estimates for a broad spectrum of ecohydrologically contrasting environments.

The statistical metrics of daily λE and H was better than the half-hourly error statistics in the semi-arid and mesic ecosystems, with RMSD 11–18 W m^{-2} (12–20 W m^{-2} for H), MAPD of 20–39% (24–37% for H), R^2 of 0.65–0.84 (0.73–0.87 for H), slope and offsets of regression to the order of 0.70–0.84 (0.67–0.79 for H) and 9–10 W m^{-2} (19–20 W m^{-2} for H), respectively (Figures 4c–4f). As for subdaily statistics, the predictive errors in daily H were lowest (12 W m^{-2} RMSD and 12% MAPD) in the arid ecosystems, whereas percent λE errors were highest (55% MAPD) (due to low mean λE) (Figures 4a and 4b). An evaluation of the annual SEB fluxes revealed a very good agreement between observed and predicted E and H , where STIC1.2 explained 97% of the measured variability, with MAPD and RMSD to the order of 10% and 55–84 mm, respectively (Figures 5a and 5b).

An intercomparison of STIC1.2 half-hourly error statistics with the two previous versions (STIC1.0 and STIC1.1) revealed maximum improvement in the performance of STIC1.2 for arid and semi-arid ecosystems (as compared to the mesic ecosystems) (Figure A1). Among the different model versions, notable differences in MAPD (20–60%, 8–40%, and 5–30%) and RMSD (25–50 W m^{-2} , 20–40 W m^{-2} , and 18–60 W m^{-2})

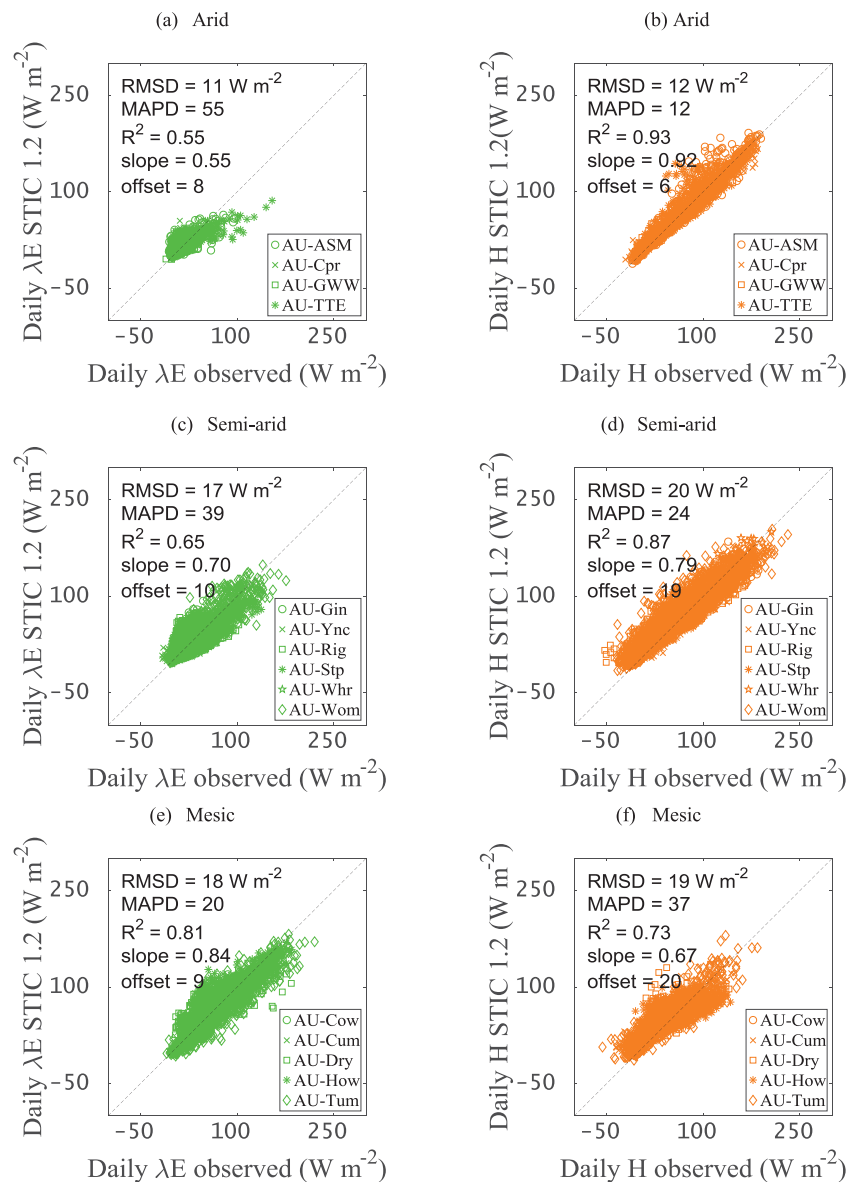


Figure 4. Comparison of daily (a, c, and e) λE and (b, d, and f) H predicted by STIC1.2 with measured SEB flux components in ecohydrologically contrasting OzFlux ecosystems of three aridity classes (as defined in Table 1). Data from the sites falling under same aridity class are combined together.

were found between STIC1.2 and STIC1.0, whereas the differences were relatively lower (5–40%, 3–22%, and 5–18% in MAPD; 3–10 W m⁻², 2–8 W m⁻², and 4–18 W m⁻² in RMSD) between STIC1.2 and STIC1.1 (Figure A1). Statistical metrics of individual site-year is given in Table A2 with description in Appendix A1.

5.2. Effects of T_R and Environmental Variables on the Performance of STIC1.2 in Different Ecosystems

Sensitivity analysis revealed that the relative change in λE error is inversely related to the relative change in T_R , thus a 10% reduction in T_R can lead up to 50% increase in percent λE error for these ecosystems (Figures 6a, 6c, and 6e) (Table 3). Maximum sensitivity of λE to T_R was found for arid and semi-arid ecosystems with significant correlations of (−0.35) to (−0.92) and (−0.30) to (−0.35) ($p < 0.05$) for soil moistures above 0.05 m³ m⁻³ and 0.10 m³ m⁻³ (Table 3), respectively. In the mesic ecosystems, the sensitivity of λE errors to T_R was relatively uniform across all the ranges of soil moisture ($r = (-0.26)$ to (-0.29) , $p < 0.05$) and E_p/ϕ ($r = (-0.27)$ to (-0.31) , $p < 0.05$) (other than conditions of extremely high evaporative potential) (Table 3). In arid and semi-arid ecosystems, the sensitivity of the λE error to T_R was confounded due to E_p/ϕ (Figures 6a and 6c) (also evident from the principal component analysis described below).

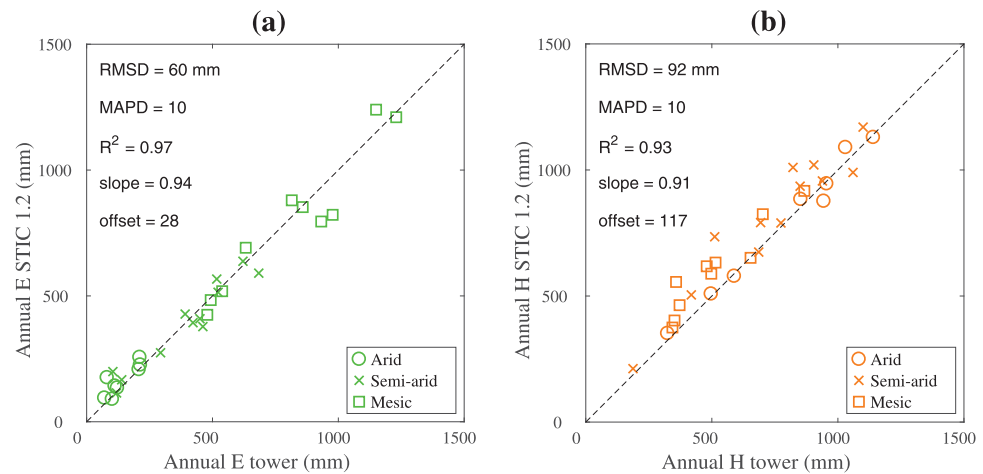


Figure 5. (a and b) Validation of STIC1.2 estimates of annual E and H against EC tower measurements. These are the annual sum of E and H for years 2013 and 2014 at each of the flux tower sites categorized according to their aridity class as defined in Table 1.

Principal component regression (PCR) of $\Delta_{\lambda E}$ versus T_R and environmental variables (ϕ , D_A , and u) revealed T_R , D_A , and ϕ to be the first principal component (PC1) affecting $\Delta_{\lambda E}$ variance in all the ecosystems (Figures 6b, 6d, and 6f). However, the relative effect of T_R in conjunction with different environmental factors in controlling the variance of $\Delta_{\lambda E}$ varied among ecosystems. Maximum PC1 loading was found for T_R and D_A followed by ϕ in arid and semi-arid ecosystems (Figures 6b and 6d) where their correlation with $\Delta_{\lambda E}$ varied between 0.70 and 0.75 (T_R), 0.65 and 0.70 (D_A) and 0.50 and 0.55 (ϕ), respectively (Figures 6b and 6d). Contrarily, in the mesic ecosystem, all the three variables had equal loadings (correlation 0.50) with $\Delta_{\lambda E}$ variance in PC1 axis (Figure 6f). The effects of wind speed (u) on the $\Delta_{\lambda E}$ variance was reflected in the second principal component (PC2) axis with correlation varying from 0.55 to 0.75. The residual errors in sensible heat flux (Δ_H) showed similar behavior of the Δ_H variance as the variance of $\Delta_{\lambda E}$ against T_R and environmental variables (not shown).

5.3. Relationship between Ecohydrological Conditions and T_R in Determining Errors and Variability of SEB Flux Components Predicted by STIC1.2

The scatter between MAPD and ecohydrological indicators in Figure 7 shows opposite relationships for λE and H . Annual E/R_N ratio and ε had the strongest impacts on the MAPD of both fluxes. As evident from the slopes of the regression lines, 1% increase in ε was found to cause approximately 17% decrease (15% increase) in $\text{MAPD}_{\lambda E}$ (MAPD_H) (Figure 7a). An increase of 10% in E/R_N would cause a 76% decrease and 55% increase in $\text{MAPD}_{\lambda E}$ and MAPD_H , respectively (Figure 7c). A systematic increase in $\text{MAPD}_{\lambda E}$ was found with increasing cV_θ , where a 10% increase in cV_θ resulted in 34% increase in $\text{MAPD}_{\lambda E}$ (Figure 7b). However, the impact of variation in θ was approximately 50% less for the accuracy of predicted H , as evident from the slope of the regression line (slope = 0.19) (Figure 7b). Interestingly, a logarithmic increase in $\text{MAPD}_{\lambda E}$ was found with increasing climatic dryness (Figure 7d). $\text{MAPD}_{\lambda E}$ varied from 18 to 30% for E_p/P ratio of 0 to 2.5 and it progressively increased from 55% to 100% when E_p/P ratio exceeded 5 (Figure 7d).

The scatter plots of monthly variances in predicted versus observed λE and H ($\sigma^2_{\lambda E}$ and σ^2_H) revealed the capacity of STIC1.2 to explain 88–90% of the observed flux variances in a broad range of aridity conditions (Figures 8a and 8b). The correlation matrix of the residual variance in the fluxes ($\Delta\sigma^2_{\lambda E} = \sigma^2_{\lambda E \text{ STIC1.2}} - \sigma^2_{\lambda E \text{ observed}}$ and $\Delta\sigma^2_H = \sigma^2_{H \text{ STIC1.2}} - \sigma^2_{H \text{ observed}}$) against a host of ecohydrological and meteorological variables revealed the absence of any strong systematic relationship between $\Delta\sigma^2_{\lambda E}$ and $\sigma^2_{T_R}$, σ^2_θ , σ^2_P ($r = \pm 0.2$) (Figure 8c). For H , the similar analysis revealed 20–40% correlation between $\Delta\sigma^2_H$ and $\sigma^2_{T_R}$, σ^2_{TA} (Figure 8d).

6. Discussion

Section 6.1 describes SEB flux prediction errors for STIC1.2 in the context of uncertainty in the relationship between T_R and aggregated moisture availability by evaluating the relationship between M , T_R , and the conductances, and thereby assessing the role of conductances estimates on residual λE error. This section also highlights the impact of SEB closure correction errors in MAPD and systematic RMSD of the predicted fluxes.

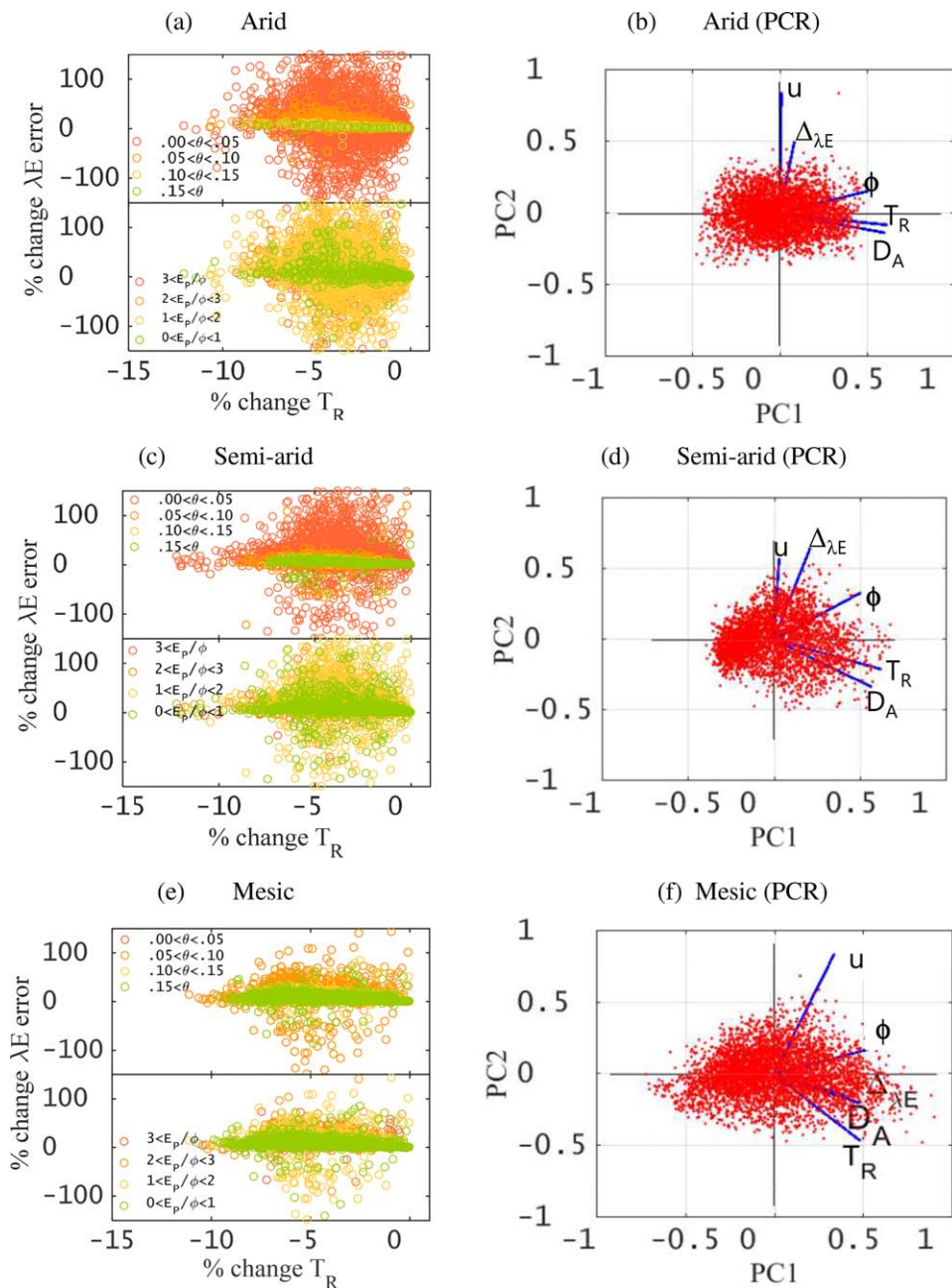


Figure 6. (a, c, and e) Scatter plots showing relative change in λE errors due to relative change in T_R in three ecosystems of contrasting aridity. (b, d, and f) Loadings of Principal Component Regression (PCR) between residual error in STIC1.2 λE ($\Delta\lambda E$) with T_R and environmental variables showing the contribution of each principal component in explaining the variance of the residual λE error. Half-hourly data are used for this analysis.

Section 6.2 discusses how the collective role of T_R and environmental variables affect the predictive errors in STIC1.2. Lastly, section 6.3 discusses the link between T_R and ecohydrological conditions in determining the error and variability of STIC1.2-based SEB flux predictions.

6.1. What is the Performance of STIC1.2 When Evaluated With High Temporal Resolution Data Across an Aridity Gradient in Australia?

6.1.1. Role of Uncertain Relationship Between M and T_R

Evaluation of STIC1.2-derived SEB fluxes at 15 Ozflux sites of broad aridity classes revealed relatively large differences between predicted and observed λE in the arid ecosystems as compared to the semi-arid and

Table 3

Sensitivity of λE Error to T_R in Three Different Types of OzFlux Ecosystems, as Shown by the Cross Correlation Between the Change in % λE Error and % Change in T_R for a Range of Soil Moisture and Potential Evaporation-Net Available Energy Ratio

θ and E_p/ϕ criteria	Class	Correlation between relative change in λE error (%) and relative change in T_R (%)		
		Arid	Semi-arid	Mesic
θ ($\text{m}^3 \text{m}^{-3}$)	$0 < \theta < 0.05$	-0.17	-0.14	-0.29
	$0.05 < \theta < 0.10$	-0.38	-0.18	-0.29
	$0.10 < \theta < 0.15$	-0.35	-0.30	-0.23
	$0.15 < \theta$	-0.92	-0.36	-0.29
E_p/ϕ ratio	$3 < E_p/\phi$	-0.16	-0.10	-0.09
	$2 < E_p/\phi < 3$	-0.18	-0.19	-0.27
	$1 < E_p/\phi < 2$	-0.17	-0.17	-0.28
	$0 < E_p/\phi < 1$	-0.14	-0.14	-0.31

Note. The bold values are moderate to high correlation and highly significant ($p < 0.05$), whereas the non-bold values are low correlation and significant ($p < 0.05$).

mesic ecosystems. Uncertainty in the relationship between T_R and aggregated moisture availability (M) could be a considerable source of error in the predictive power of STIC1.2 in the water-limited ecosystems. In STIC1.2, M is modeled as a fraction of the dewpoint temperature difference between evaporating front and atmosphere ($T_{OD} - T_D$) and of infrared temperature—dewpoint differences between surface to atmosphere ($T_R - T_D$). These two factors were weighted by two different slopes of saturation vapor pressure-temperature relationships (s_1 and s_2 ; equation (S26)) (Mallick et al., 2016). This implies that for constant available moisture, this fraction is constant. However, even for varying ϕ , D_A , and T_A , constant moisture availability does not imply invariant $(T_{OD} - T_D)/(T_R - T_D)$ because a wet surface has a different sensitivity to these variables than a dry surface with limited surface conductance. Due to $\phi - D_A - T_R$ feedbacks (Zhang et al., 2014), $T_{OD} - T_D$ can actually decrease with increasing T_R , ϕ , and D_A , whereas $T_R - T_D$ would increase. In this context, estimation of T_{OD} plays a critical role in arid and semi-arid environments, which further requires sound estimation of s_1 . From the definition of s_1 $[(e_0 - e_A)/(T_{OD} - T_D)]$, $e_0 \rightarrow e_A$ and $s_1 \rightarrow 0$ for an extremely dry surface with insignificant evaporation. In the present

case, the estimates of s_1 as a function of T_D tend to be higher than the possible s_1 -limits in water-limited environments, which is likely to introduce errors in T_{OD} estimation (through supporting information equation (S27)). Overestimation of s_1 would also lead to an overestimation of M (through the denominator in supporting information equation (S26)), thus leading to overestimation of the conductances and λE . As seen in Figures 9a, 9c, and 9d), the relationship between M and T_R is very strong for low magnitudes of M ($M < 0.025$ for arid ecosystem; $M < 0.10$ for semi-arid and mesic ecosystems), and a significantly strong

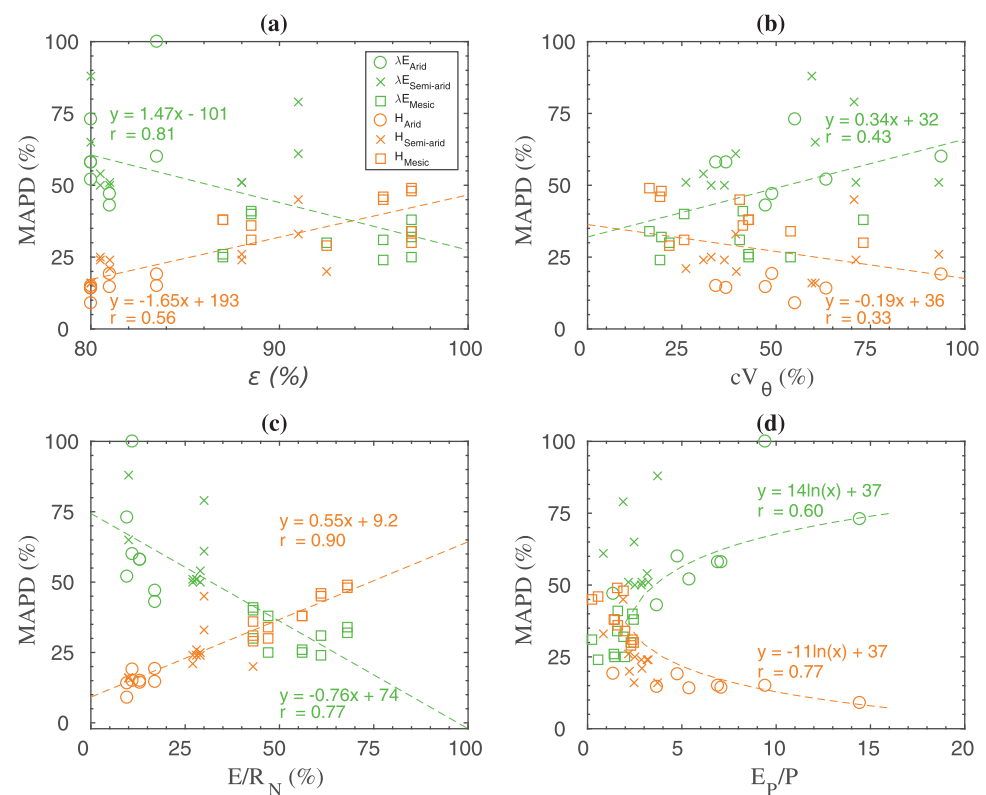


Figure 7. (a–d) Scatters between MAPD in daily λE and H versus ecohydrological and land surface variables combining data from 15 OzFlux ecosystems representing three broad aridity classes as described in Table 1.

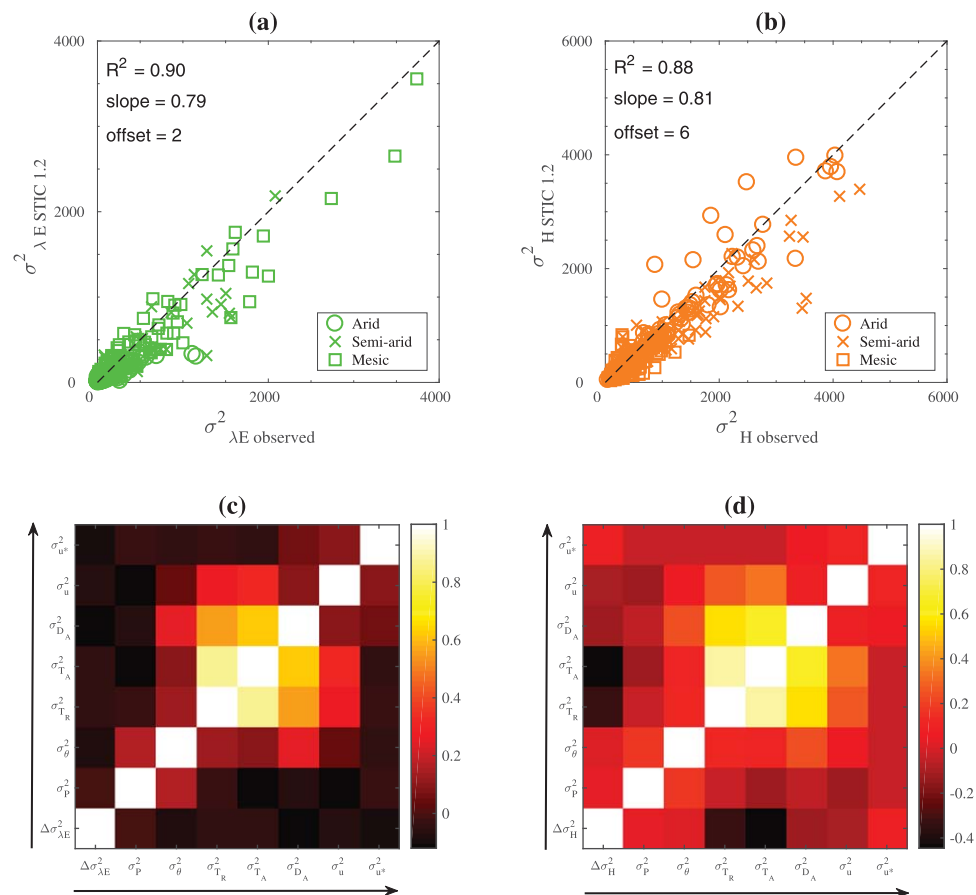


Figure 8. (a and b) Scatters of monthly variance of STIC1.2 versus observed λE ($\sigma^2_{\lambda E}$) and H (σ^2_H) in contrasting OzFlux ecosystems representing three broad aridity classes as defined in Table 1. (c and d) Correlation matrix showing the relationship between the residual variances in λE ($\partial\sigma^2_{\lambda E} = \sigma^2_{\lambda E \text{ STIC1.2}} - \sigma^2_{\lambda E \text{ observed}}$) and H ($\partial\sigma^2_H = \sigma^2_{H \text{ STIC1.2}} - \sigma^2_{H \text{ observed}}$) versus ecohydrological and meteorological variables.

relationship is also evident between g_C/g_A versus M ($r = 0.81\text{--}0.88$; $p < 0.05$) in all the ecosystems when the surface is substantially dry ($M < 0.15$). g_C/g_A ratios tend to be invariant with increasing moisture availability in the mesic ecosystems ($M > 0.25$; Figure 9e). Therefore, critical errors could be introduced in λE retrieval under dry surface conditions due to the strong association between M and T_R , and dependence of the conductances on M . Residual error analysis of λE versus both the conductances revealed λE error to be fairly correlated with g_A and g_C in the sparsely vegetated arid and semi-arid ecosystems (Figures 9b and 9d) ($r = 0.30\text{--}0.40$, $p < 0.05$; $r = 0.28\text{--}0.32$, $p < 0.05$). There was a general tendency to overestimate λE when g_C was very low, which was eventually reduced with increasing g_C . Residual λE error appears to be heteroscedastic with g_A , which signifies unequal variability of λE error across a range of g_A . A weak relationship between residual λE error and conductances was found in the mesic ecosystem (Figure 9f), resulting in small predictive errors in λE for this ecosystem.

Significantly lower errors in predicting H than λE might be the result of partial compensation of g_A/g_C in both numerator and denominator of the PM formulation for H (equation (4b)) (Winter & Eltahir, 2010). In our study, g_C showed much more variability as a function of T_R ($r = 0.72\text{--}0.74$; 1% change in T_R would lead to 5.2–7.5% change in g_C) than did g_A with T_R ($r = 0.26\text{--}0.65$; 1% change in T_R would lead to 1.6–2% change in g_A) (Figure 10), suggesting that error in g_C was larger than error in g_A . Compensation of conductance errors in computing H (equation (4b)) might have resulted in substantial compensation of H errors in all the ecosystems. By contrast, combined uncertainty due to g_A in the numerator of equation (4a) with uncompensated g_A/g_C in the denominator of equation (4a) (Mallick et al., 2015; Winter & Eltahir, 2010) resulted large disagreements in measured and modeled λE for the arid and semi-arid ecosystems where λE was small.

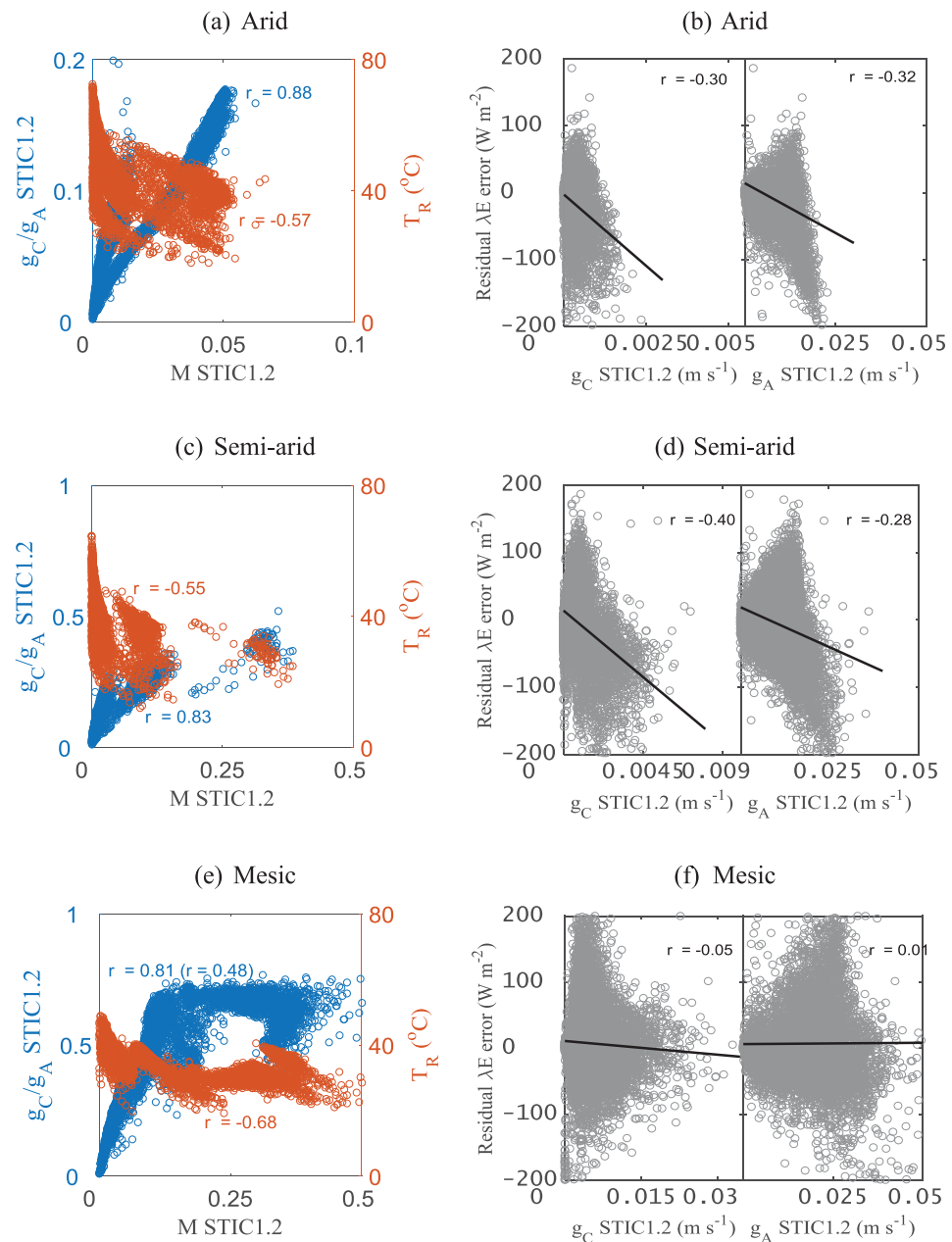


Figure 9. (a, c, and e) Scatter plots showing the relationship between g_C/g_A versus M and M versus T_R as modeled in STIC1.2 for different ecosystem types. (b, d, and f) Scatter plots showing how the residual λE error in STIC1.2 is affected by q_C and q_A for different types of aridity classes.

6.1.2. Role of SEB Closure on Statistical Metrics

Differences between STIC1.2 versus observed λE may be partly attributed to the BREB-closure correction of λE observations. Although Bowen ratio correction forces SEB closure, in the arid and semi-arid ecosystems major corrections are generally observed in H , whereas λE is negligibly corrected (Chávez et al., 2005). Significant correlations are found between the λE error statistics and BREB-closure corrections ($r = 0.60$ for MAPD in Figure 11a, $r = 0.66$ for $\text{RMSDs}^2/\text{RMSD}^2$ in Figure 11b). In majority of the arid and semi-arid sites, high MAPD and $\text{RMSDs}^2/\text{RMSD}^2$ in λE ($>50\%$) was associated with low percent of closure correction in λE (12–20%) (Figures 11a and 11b). Both the error metrics were relatively high when modeled λE was compared against RES-closure-based λE observations; however, RES-closure revealed a substantially weaker relationship between errors and percent closure corrections than in BREB-closure (Figures 11c and 11d).

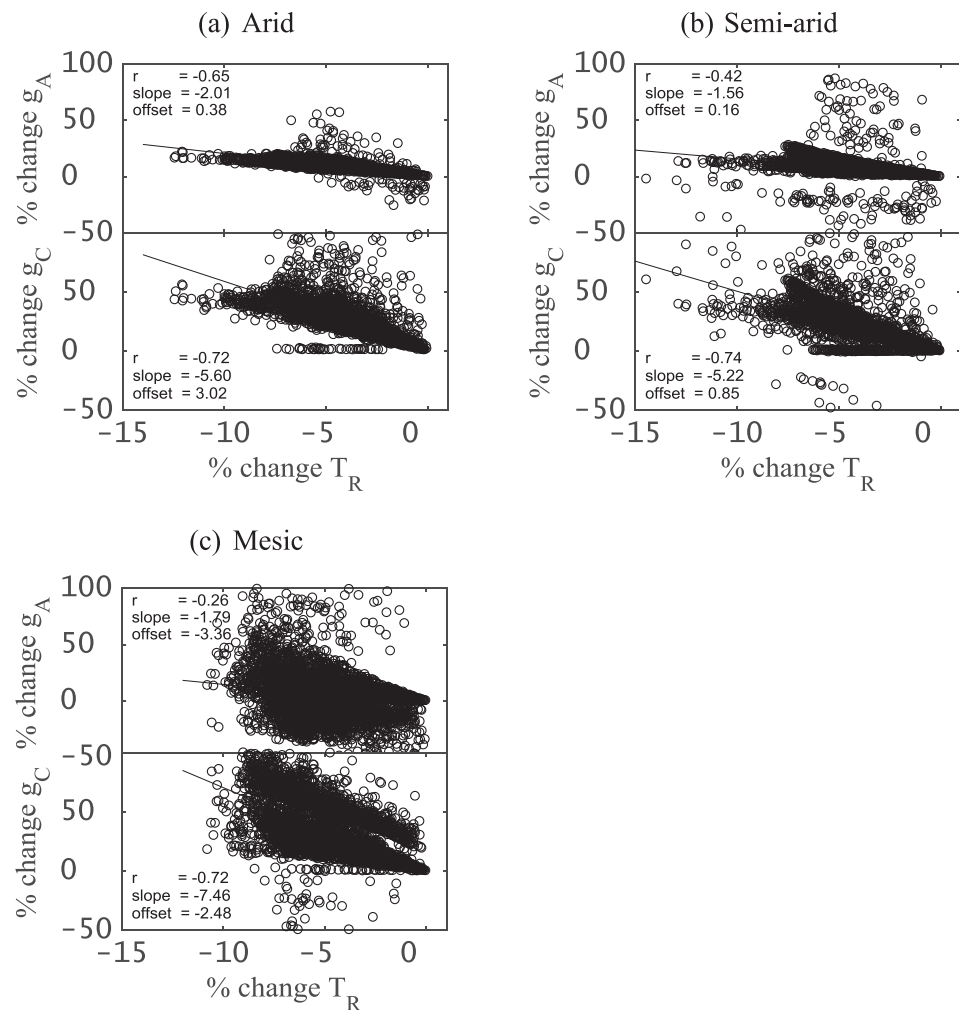


Figure 10. Scatter plots showing the sensitivity of g_C and g_A to T_R as modeled in STIC1.2 in three different classes of ecosystems. This shows the relative change in the individual conductances due to the relative change in T_R .

BREB-closure correction was found to fail under hot, dry conditions in some previous studies. This is due to the combination of extremely high evaporative potential and sensible heat entrainment from boundary layer desaturating the surface and causing the surface-to-air vapor pressure gradient to reverse (Mallick et al., 2014b; McHugh et al., 2015; Perez et al., 1999), a condition that prevails in the arid and semi-arid ecosystems during most part the year. The assumption of scalar similarity for heat and water vapor is violated in these conditions and g_A of heat flux can be two to three times higher than g_A of the water vapor flux (Katul et al., 1995). For the RES-closure, additional uncertainty in λE might be introduced due to neglecting subsurface heat sink in G measurements (Heitman et al., 2010), which themselves can have errors of 18–66% (Ochsner et al., 2006). Similar analysis of H revealed relatively low overall correlation ($r = 0.41$) between MAPD of predicted H and SEB closure (Figures 11e and 11f), with a tendency of high MAPD in mesic sites due to overcorrection of H . This is due to the fact that g_A responsible for H might be lower than g_A of λE in mesic ecosystems and the assumption of scalar similarity for heat and water vapor may not be true. For a similar reason, the use of Bowen ratio approximations in the state equation of T_0 in STIC1.2 might also be responsible for additional error propagation in all the three ecosystems.

6.2. How Do T_R and Associated Environmental Variables Affect the Performance of STIC1.2 in Different Ecosystems?

The relationship between the relative change in λE error with the relative change in T_R above a threshold soil moisture content in arid and semi-arid ecosystems (Figures 6a, 6c, and 6e; Table 3) indicates the critical

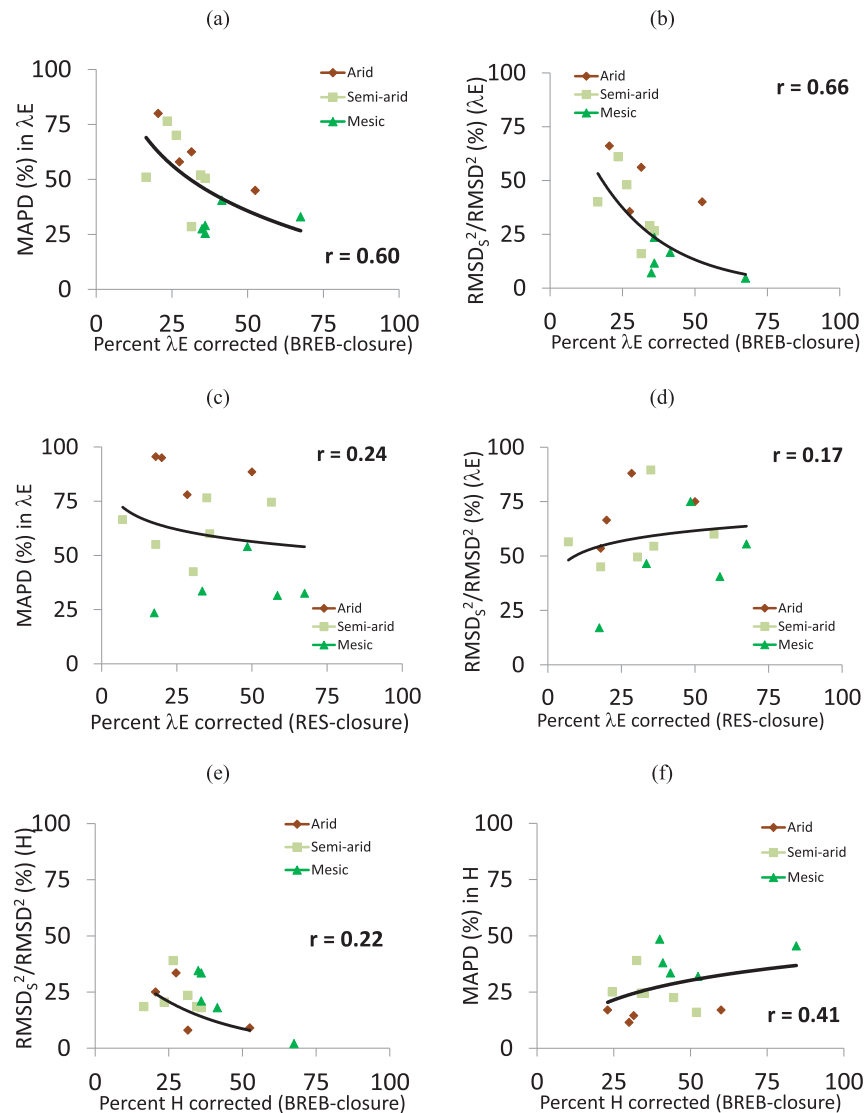


Figure 11. (a–d) Scatters of MAPD and $RMSD_s^2/RMSD^2$ in half-hourly λE predicted by STIC1.2 versus average percent of BREB-closure corrected λE and RES-closure corrected λE measured with the EC method. (e and f) Scatters of MAPD and $RMSD_s^2/RMSD^2$ in half-hourly H predicted by STIC1.2 versus average percent of BREB-closure corrected H measured with the EC method. Data from 15 OzFlux sites falling under three classes of contrasting aridity (as in Table 1) are grouped. Relative λE and H correction (in percent) is computed as, $\% \lambda E \text{ correction} = 100 * (\lambda E_{\text{corrected}} - \lambda E_{\text{uncorrected}}) / \lambda E_{\text{uncorrected}}$ and $\% H \text{ correction} = 100 * (H_{\text{corrected}} - H_{\text{uncorrected}}) / H_{\text{uncorrected}}$. Here $\lambda E_{\text{corrected}}$ and $H_{\text{corrected}}$ are the Bowen ratio corrected λE ($\lambda E_{\text{uncorrected}}$) and H ($H_{\text{uncorrected}}$) observations.

role of uncertainty in T_R -soil moisture relationship in STIC1.2 and the role of M in controlling g_C/g_A and resultant λE errors in the water-limited ecosystems, as discussed previously. As further evident from Figures 6b, 6d, and 6f), while the accumulated effects of T_R and D_A were predominant in explaining $\Delta_{\lambda E}$ variance in arid and semi-arid ecosystems, the influence of ϕ was comparable to T_R and D_A in explaining $\Delta_{\lambda E}$ variance in the mesic ecosystems. Since T_R controls the atmospheric humidity profile by constraining soil moisture, g_C and transpiration; T_R and D_A have stronger autocorrelation in arid and semi-arid ecosystems as compared to the mesic ecosystems (Abdi et al., 2017; Crago & Qualls, 2014); and λE is mainly limited by combination of these two surface and atmospheric moisture variables. This explains the dominant role of T_R and D_A in controlling the maximum $\Delta_{\lambda E}$ variance as reflected in the high correlation (0.65–0.75) in the first principal component (PC1) axis of arid and semi-arid ecosystems (Figures 6b and 6d). In contrast, E in mesic ecosystems is constrained by T_R , ϕ , and D_A ; and all the three variables had accumulated impact in explaining the relative error

change in λE (Table 3 and Figure 6e) and $\Delta_{\lambda E}$ variance as seen in the PC1 axis in this ecosystem (Figure 6f). Since PC1 had the highest total variance in all the ecosystems, its variables are the most important in determining the predictive errors in λE . The effects of wind speed (u) in explaining $\Delta_{\lambda E}$ variance (as seen in PC2) might originate from some collinearity of u with net radiative heating, T_R and D_A as earlier reported by Mallick et al. (2016).

6.3. Is There an Association between Ecohydrological Conditions and T_R in Determining the Errors and Variability of SEB Flux Components Predicted by STIC1.2?

Given the critical role of T_R in STIC1.2, the estimate of T_R is an additional source of error (through ε) in predicted λE and H for the individual study sites (Figure 7a) and the error is consequently propagated into the MAPD of λE and H versus cV_{θ} , annual E/R_N , and E_p/P relationships (Figures 7b–7d). Low annual E/R_N and high annual E_p/P are the indicators of water limitations, where low E is the result of low P and θ despite an abundance of available energy in conjunction with high potential evaporative demand. Such water limitations make E very sensitive to soil moisture variations (Jarvis & McNaughton, 1986), thereby accelerating biophysical feedbacks on E (Mallick et al., 2016; Siqueira et al., 2008), and the rate of change of E becomes directly proportional to the canopy (or surface) conductance (g_C) (Jarvis & McNaughton, 1986). Since our g_C estimates are inevitably constrained by T_R (through M), accuracy of T_R is a key factor for enhancing E retrievals under these conditions.

Given ε appears in the denominator of the T_R retrieval equation, T_R is extremely sensitive to the uncertainties in ε (Hulley et al., 2012). Underestimation (overestimation) of T_R would lead to overestimation (underestimation) of M , which further leads to underestimation (overestimation) of g_A/g_C in the denominator of the PM model, causing the resultant SEB flux estimations to become uncertain. Careful handling of diurnal variations of infrared ε is therefore essential for deriving accurate surface skin temperature (Hulley et al., 2012; Li et al., 2007). Substantial diurnal variations in ε are found in arid and semi-arid ecosystems due to the influence of soil moisture (θ) (Hulley et al., 2010; Masiello et al., 2014). For low values of θ , the rate of change of ε per unit change of θ (i.e., $\partial\varepsilon/\partial\theta$), at wave numbers of reststrahlen absorption is considerably large (Masiello et al., 2014; Mira et al., 2007); $\partial\varepsilon \approx 0.05$ per $\partial\theta$ of 0.01 kg kg^{-1} . Consequently, exclusion of sub-daily and seasonal variation of ε in the T_R estimation is evident in MAPD of λE versus ε scatter plots (Figure 7a).

Despite the absolute differences between the predicted and observed SEB fluxes, very good agreement between the flux variances (Figures 9a and 9b) indicates the ability of STIC1.2 to capture the radiation and water driven variabilities in SEB fluxes from mesic to arid ecosystems. The correlation of ± 12 – 15% between $\Delta\sigma_{\lambda E}^2$ and σ_{θ}^2 , $\sigma_{P_r}^2$, and $\sigma_{T_R}^2$ (Figure 9c) is a result of aforementioned (section 6.1) T_R uncertainties, in conjunction with SEB closure correction errors of EC λE observations in arid and semi-arid environments. Besides, the negative relationship ($r = -0.20$) between $\Delta\sigma_{\lambda E}^2$ ($\sigma_{\lambda E \text{ STIC1.2}}^2 - \sigma_{\lambda E \text{ observed}}^2$) versus $\sigma_{u^*}^2$ is most likely associated with the collinearity between wind shear and T_R , D_A , and ϕ (also reported in Mallick et al., 2016) as described in section 6.2. Nearly zero correlation between $\Delta\sigma_H^2$ with ecohydrological variances further indicates that H was predominant in water-limited regions, and sensible heat flux is the primary pathway by which ecohydrological variances induces variations in atmospheric variables and consequently affects the boundary layer growth (Koster et al., 2015). This was also supported by 40% correlation between $\Delta\sigma_H^2$ and $\sigma_{T_A}^2$. Also the absence of a relationship between $\Delta\sigma_H^2$ and σ_u^2 indicates that the exclusion of wind speed from STIC1.2 (see equations (5)–(8)) does not significantly affect the SEB flux estimates. This error characterization in a broad range of ecohydrological conditions also indicated that in the ecosystems with low annual evaporative index (E/R_N) and very high climatic dryness index (E_p/P), the thermal component of the SEB fluxes (i.e., H) is dominant and should be given emphasis to assess model performance (Dirmeyer, 2011; García et al., 2008).

The overall RMSD of 25–61 and 11–37 W m^{-2} in half-hourly and daily SEB fluxes and the associated statistical metrics are comparable with the results reported in a host of SEB modeling studies that uses empirical sub-models to parameterize the conductances. Using the two-source energy balance model (TSEB) (Norman et al., 1995), some recent studies have reported RMSD to the order of 72–135 and 52–131 W m^{-2} in hourly λE and H for a semi-arid grassland in Spain (Kustas et al., 2016), 95–166 W m^{-2} in hourly λE (Song et al., 2016) to 45–50 W m^{-2} in daily λE for semi-arid irrigated cotton in Texas and Arizona (Colaizzi et al., 2014; French et al., 2015), and 50–59 W m^{-2} in hourly λE for irrigated maize in China (Song et al., 2016). A variant of TSEB model (SPARSE model) is found to produce 43–47 W m^{-2} in instantaneous λE and 50–80 W m^{-2} in

hourly λE in Tunisia and Morocco (Boulet et al., 2015; Saadi et al., 2017). Considering the error statistics of state-of-the-art SEB models and their parameterization uncertainties (Timmermans et al., 2013); the performance of STIC1.2 indicates substantial potential of this model towards bridging thermal infrared sensing and physically-based evapotranspiration modeling. An intercomparison of STIC1.2 with other SEB models is beyond the scope of this manuscript. However, a recent study on regional evapotranspiration mapping demonstrated a comprehensive intercomparison of STIC1.2 with two other global models across an aridity gradient in the conterminous United States for contrasting rainfall years as well as on a wide variety of biomes (Bhattarai et al., 2018). The study revealed better performance of STIC1.2 as compared to the other models and also demonstrated the critical role of conductances and associated land surface parameterizations on the model errors, intermodel agreements, and disagreements.

A host of literatures reported measurement uncertainties in H and λE to the order of ± 15 – 20 and ± 35 – 50 W m^{-2} (Masseroni et al., 2014; Wang et al., 2015). These uncertainties are associated with high magnitude of net radiation (Hollinger & Richardson, 2005), and with stochastic nature of turbulence (Hollinger & Richardson, 2005; Wang et al., 2015). Landscape heterogeneity may induce large scale turbulence which consequently leads to large H and λE uncertainty in arid and semi-arid ecosystems (Wang et al., 2015). However, it is unlikely that the entire RMSD in λE and H is attributable solely to the EC measurement uncertainties (Foken, 2008). As a result, the range of RMSD obtained between STIC1.2 and tower H and λE is likely to be determined by the combination of structural uncertainties in STIC1.2 and SEB flux measurement uncertainties in the EC towers.

7. Conclusions

By integrating thermal infrared temperature into a combined structure of Penman-Monteith and Shuttleworth-Wallace framework we show the promise of a single-source box modeling approach towards bridging thermal infrared sensing and physically-based model to retrieve the energy-water fluxes. Analysis of STIC1.2 results in 15 eddy covariance sites across an aridity gradient in Australia led us to the following conclusions.

1. STIC1.2 overcomes the uncertainties in aerodynamic temperature and biophysical conductances parameterizations, and establishes a direct feedback of T_R on SEB fluxes, source/sink height temperature and vapor pressures, and the conductances. The efficiency of STIC1.2 to explain the variances of half-hourly to annual SEB fluxes across diverse biomes and ecohydrological settings in Australia indicates the skill of the model to capture the water-energy flux variabilities in hydrological extremes.
2. Uncertainty in the relationship between T_R and moisture availability (M) is a considerable source of error in the predictive power of STIC1.2 in the water-limited ecosystems. Use of differential T_R observations (between sunrise and noontime) as a water stress constraint could potentially diminish the uncertainty in M and eventually SEB flux prediction errors in STIC1.2. Besides, the performance of STIC1.2 depends on rigorous surface emissivity (ε) corrections, particularly in arid and semi-arid ecosystems. Since ε is sensitive to the soil water content variations, assuming a constant surface emissivity for retrieving T_R significantly affects the predictive skills of STIC1.2 in those ecosystems where substantial variations in soil moisture are observed. Spectrometer-based measurements representing appropriate footprint area around EC sites are needed to capture the diurnal variations in ε for an improved T_R retrieval.
3. Disparities between predicted and observed λE in arid semi-arid ecosystems also emerged due to the surface energy balance closure (SEB) correction errors of λE observations. A robust SEB closure correction is needed for better interpretation of the predictive capacity of STIC1.2 in water-limited ecosystems.
4. In the arid ecosystems where evapotranspiration (E) signal is small, the thermal component of the energy-water fluxes is predominant and sensible heat flux (H) tends to be a better metric to test the skill of any physically-based model, and might be a favored water stress indicator. Simultaneously, in the semi-arid and mesic ecosystems, both E and H appear to be the better metric in detecting the water cycle variability, and STIC1.2 showed substantial promise to capture the magnitude and variabilities of these two most important energy-water cycle components across these broad aridity classes.
5. T_R is the most critical variable explaining the error variance of E in arid and semi-arid ecosystems, while both net available energy and T_R explain the error variance of E in mesic ecosystems. Effects of ecohydrological conditions in determining the predictive capacity of STIC1.2 are also associated with T_R and radiation driven SEB flux variability in the two ecohydrological extremes.

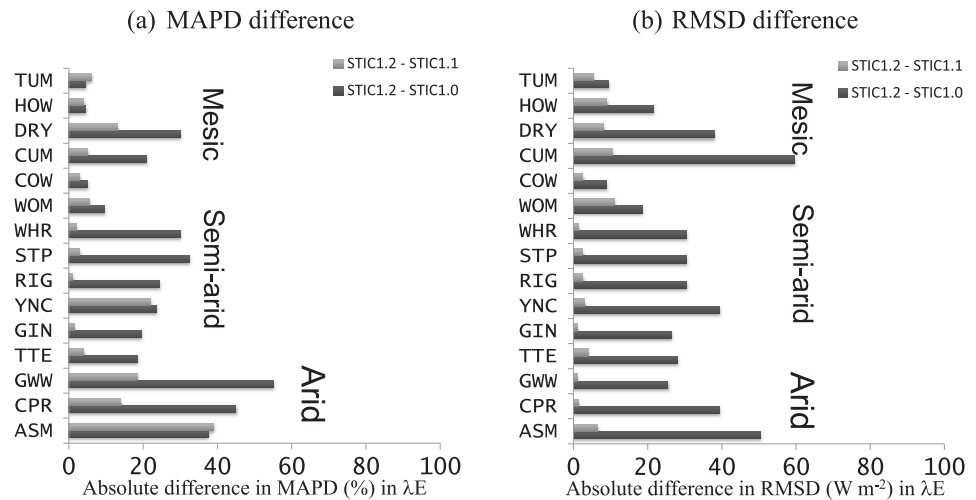


Figure A1. (a) Difference in MAPD (%) in λE between STIC1.2 versus STIC1.1 and STIC1.0 for the 15 OzFlux sites, (b) Difference in RMSD ($W m^{-2}$) in λE between STIC1.2 versus STIC1.1 and STIC1.0 for the 15 OzFlux sites.

STIC1.2 is independent of any biome specific or leaf-scale empirical parameterizations of the conductances, which implies that it does not require any data on plant functional types or vegetation structure. This model is a valuable addition to the recent Australian energy and water exchange research initiative (OzEWEX), in particular to the WG2 (working group 2) that focuses on observations to evaluate and compare biophysical models and data products describing energy and water cycle variables. Given the significance of aerodynamic and canopy conductances in characterizing the land-atmosphere interactions, STIC1.2 can be used to study the ecohydrological feedbacks on land surface versus boundary layer interactions. With the availability of accurate T_R information from new MOD21 land surface temperature (Hulley et al., 2015), LANDSAT, recently launched Sentinel-3, or future missions with thermal sensors like HypsIRI, a successful application of STIC1.2 is expected for mapping regional-scale vegetation water use with special emphasis in the water-limited ecosystems.

Appendix A

A1. Intercomparison of STIC1.2 With STIC1.0 and STIC1.1

An intercomparison of STIC1.2 error statistics with the previous two versions of STIC (STIC1.0 and STIC1.1) revealed maximum improvement in the performance of STIC1.2 in arid and semi-arid ecosystems (as

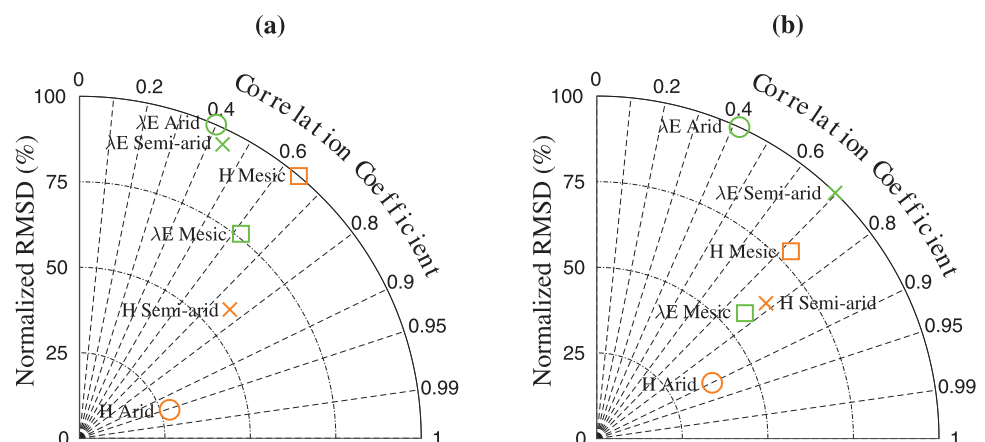


Figure A2. Taylor diagram of daily error statistics showing the normalized RMSD and correlation coefficient between observed and predicted λE and H during (a) dry and (b) wet seasons of 2013–2014 in ecohydrologically contrasting OzFlux ecosystems of three aridity classes as defined in Table 1. Data from the sites falling under same aridity class are combined.

Table A1
Variables and Symbols and Their Description Used in the Present Study

Variables and symbol	Description
λE	Evapotranspiration (evaporation + transpiration) as latent heat flux (W m^{-2})
H	Sensible heat flux (W m^{-2})
R_N	Net radiation (W m^{-2})
G	Ground heat flux (W m^{-2})
ϕ	Net available energy (W m^{-2}) (i.e., $R_N - G$)
$R_{S\downarrow}$	Downwelling shortwave radiation (W m^{-2})
$R_{S\uparrow}$	Upwelling shortwave radiation (W m^{-2})
$R_{L\downarrow}$	Downwelling longwave radiation (W m^{-2})
$R_{L\uparrow}$	Upwelling longwave radiation (W m^{-2})
ε	Thermal infrared surface emissivity
T_A	Air temperature ($^{\circ}\text{C}$)
T_D	Dewpoint temperature ($^{\circ}\text{C}$)
T_R	Radiometric surface temperature ($^{\circ}\text{C}$)
T_0	Aerodynamic temperature or source/sink height temperature ($^{\circ}\text{C}$)
T_{0D}	Dew-point temperature at the source/sink height ($^{\circ}\text{C}$)
R_H	Relative humidity (%)
e_A	Atmospheric vapor pressure at the level of T_A measurement (hPa)
D_A	Atmospheric vapor pressure deficit at the level of T_A measurement (hPa)
e_S	vapor pressure at surface (hPa)
e_S^*	Saturation vapor pressure at surface (hPa)
e_0	Vapor pressure at the source/sink height (hPa)
e_0^*	Saturation vapor pressure at the source/sink height (hPa)
D_0	Vapor pressure deficit at the source/sink height (hPa)
u	Wind speed (m s^{-1})
u^*	Friction velocity (m s^{-1})
s	Slope of saturation vapor pressure versus temperature curve (hPa K^{-1}) (estimated at T_A)
s_1	Slope of the saturation vapor pressure and temperature between $(T_{SD} - T_D)$ versus $(e_0 - e_A)$ (approximated at T_D) (hPa K^{-1})
s_2	Slope of the saturation vapor pressure and temperature between $(T_R - T_D)$ versus $(e_S^* - e_A)$ (hPa K^{-1})
s_3	Slope of the saturation vapor pressure and temperature between $(T_R - T_{SD})$ versus $(e_S^* - e_S)$ (approximated at T_R) (hPa K^{-1})
s_0	Slope of the saturation vapor pressure and temperature between $(T_0 - T_A)$ versus $(e_0^* - e_A^*)$ (approximated as s) (hPa K^{-1})
κ	Ratio between $(e_0^* - e_A)$ and $(e_S^* - e_A)$
E	Evapotranspiration (evaporation + transpiration) as depth of water (mm)
λE_P	Potential evaporation as flux (W m^{-2})
λE_T^*	Potential transpiration as flux (W m^{-2})
λE_W	Wet environment evaporation as flux (W m^{-2})
λE_P^*	Potential evaporation as flux according to Penman (W m^{-2})
λE_{PM}^*	Potential evaporation as flux according to Penman-Monteith (W m^{-2})
λE_{PT}^*	Potential evaporation as flux according to Priestley-Taylor (W m^{-2})
E_P	Potential evaporation as depth of water (mm)
E_P^*	Potential evaporation as depth of water according to Penman (mm)
E_{PM}^*	Potential evaporation as depth of water according to Penman-Monteith (mm)
E_{PT}^*	Potential evaporation as depth of water according to Priestley-Taylor (mm)
E_W	Wet environment evaporation as depth of water (mm)
g_A	Aerodynamic conductance (m s^{-1})
g_M	Momentum conductance (m s^{-1})
g_C	Canopy (surface) conductance (m s^{-1})
g_{Cmax}	Maximum canopy (surface) conductance (m s^{-1}) ($= g_C/M$)
M	Aggregated surface moisture availability (0–1)
λ	Latent heat of vaporization of water ($\text{J kg}^{-1} \text{K}^{-1}$)
z_R	Reference height (m)
z_{OM}	Effective source-sink height (roughness length) of momentum (m)
z_{OH}	Effective source-sink height (roughness length) of heat (m)
d_0	Displacement height (m)
γ	Psychrometric constant (hPa K^{-1})

Table A1. (continued)

Variables and symbol	Description
ρ	Density of air (kg m^{-3})
c_p	Specific heat of dry air ($\text{MJ kg}^{-1} \text{K}^{-1}$)
Λ	Evaporative fraction (unitless)
β	Bowen ratio (unitless)
α	Priestley-Taylor parameter (unitless)
q	Stefan-Boltzmann constant ($5.670373 \times 10^{-8} \text{ W m}^{-2} \text{K}^{-4}$)

compared to mesic ecosystems) for both the SEB fluxes (Table A2). Statistical metrics of STIC1.0 and STIC1.1 (Table A2) revealed substantially higher RMSD ($53\text{--}90 \text{ W m}^{-2}$ and $36\text{--}49 \text{ W m}^{-2}$) and MAPD (91–100% and 60–100%), and lower R^2 (0.23–0.64 and 0.28–0.67) as compared to STIC1.2 in arid ecosystems. In the semi-arid ecosystems, these statistics were $59\text{--}91 \text{ W m}^{-2}$ and $43\text{--}73 \text{ W m}^{-2}$ (RMSD); 31–100% and 28–100% (MAPD); and 0.19–0.84 and 0.21–0.84 (R^2), respectively.

A2. Dry Season Versus Wet Season Statistics in SEB Fluxes

The Taylor diagram (Figure A2) reveals overall lower percentage errors in H as compared to λE in arid and semi-arid ecosystems during both dry and wet seasons (please see Table A3 for dry and wet season), with

Table A2

Error Statistics of Sub-daily λE and H Derived With STIC1.0 and STIC1.1 in 15 EC Sites Covering Three Ecohydrologically Contrasting OzFlux Ecosystems of Different Aridity Classes as Defined in Table 1

Aridity class	Site name	STIC versions	λE				H			
			RMSD (W m^{-2})	R^2	MAPD (%)	RMSDs ² /RMSD ² (%)	RMSD (W m^{-2})	R^2	MAPD (%)	RMSDs ² /RMSD ² (%)
Arid ($0 < AI < 0.2$)	AU-ASM	STIC1.0	76–90	0.23–0.54	98–100	38–39	76–96	0.96–0.97	31–37	80–87
		STIC1.1	36	0.28–0.62	70–100	20–40	36	0.97–0.98	14–15	11–60
	AU-Cpr	STIC1.0	58–76	0.29–0.30	97–100	32–34	58–76	0.95–0.96	31–34	87–90
		STIC1.1	26–32	0.36–0.38	70–74	25–38	26–32	0.96–0.97	14–15	21–28
	AU-GWW	STIC1.0	53–66	0.46–0.56	91–100	19–35	53–66	0.92–0.95	28–30	69–82
		STIC1.1	33–35	0.53–0.60	60–67	37–59	33–35	0.94–0.96	14–20	6–8
Semi-arid ($0.2 < AI < 0.5$)	AU-TTE	STIC1.0	57–71	0.26–0.64	97–100	33–46	57–71	0.90–0.95	32–35	68–89
		STIC1.1	31–49	0.35–0.67	68–100	37–77	31–49	0.88–0.97	15–23	4–42
	AU-Gin	STIC1.0	77–83	0.50–0.51	66–77	16–20	77–83	0.86–0.89	33–34	71–77
		STIC1.1	54–55	0.53–0.55	53–54	40–53	54–55	0.90–0.91	24–26	14–15
	AU-Ync	STIC1.0	73–76	0.19–0.26	95–100	35–40	73–76	0.90–0.95	33–34	79–85
		STIC1.1	35–41	0.21–0.25	97–100	36–57	35–41	0.93–0.97	15–19	19–25
	AU-Rig	STIC1.0	89–91	0.30–0.33	89–100	22–29	89–91	0.78–0.81	46–60	76–77
		STIC1.1	61–63	0.35–0.43	59–79	59–65	61–63	0.85–0.86	30–45	23–37
	AU-Stp	STIC1.0	70–85	0.65–0.69	82–85	36–50	70–85	0.86–0.89	38–41	86–87
		STIC1.1	46–53	0.75–0.78	52–56	54–60	46–53	0.86–0.87	24–26	6–13
	AU-Whr	STIC1.0	66–84	0.49–0.54	73–88	14–22	66–84	0.90–0.91	30–35	72–80
		STIC1.1	43–44	0.56–0.58	52–53	30–50	43–44	0.93–0.94	21–22	15–21
Mesic ($0.5 < AI$)	AU-Wom	STIC1.0	59–72	0.83–0.84	31–45	9–39	59–72	0.90–0.93	30–32	56–81
		STIC1.1	43–73	0.78–0.84	28–40	39–67	43–73	0.89–0.94	20–38	16–35
	AU-Cow	STIC1.0	44–59	0.84–0.90	28–37	3–13	44–59	0.77–0.78	44–52	56–78
		STIC1.1	43–47	0.86–0.92	28–29	12–49	43–47	0.81–0.82	43–53	14–20
	AU-Cum	STIC1.0	87–135	0.71–0.78	60–63	28–54	87–135	0.85–0.86	46–53	86–94
		STIC1.1	49–71	0.76–0.84	34–37	5–26	49–71	0.90–0.91	25–33	40–62
	AU-Dry	STIC1.0	93–101	0.70–0.73	57–61	28–29	93–101	0.80–0.81	46–47	83–87
		STIC1.1	65–69	0.77–0.81	41–42	48–59	65–69	0.81–0.82	33–34	9–11
	AU-How	STIC1.0	77–80	0.84–0.85	29–30	13–20	77–80	0.77–0.78	45–50	83–87
		STIC1.1	60–72	0.86–0.88	26–33	27–54	60–72	0.78–0.80	40–49	9–19
	AU-Tum	STIC1.0	63–64	0.86–0.87	28–29	4–8	63–64	0.85–0.86	37–38	52–56
		STIC1.1	58–62	0.85–0.86	26–27	10–14	58–62	0.84–0.86	35–37	13–15

Table A3

Dry and Wet Seasons of the 15 OzFlux EC Sites Used in the Present Study

Aridity class	Site name	Season (months)		
Arid ($0 < AI < 0.2$)	AU-ASM AU-GWW AU-TTE	Wet Jan to Apr	Dry May to Oct	Wet Nov to Dec
		Jan to May	Jun to Oct	Nov to Dec
		Jan to Feb	Mar to Oct	Nov to Dec
Semi-arid ($0.2 < AI < 0.5$)	AU-Cpr	Dry Jan to Mar	Wet Apr to Sep	Dry Oct to Dec
		Wet Jan to Mar	Dry Apr to Oct	Wet Nov to Dec
	AU-Stp	Dry Jan to Apr	Wet May to Oct	Dry Nov to Dec
		Jan to Mar	Apr to Sept	Oct to Dec
		Jan to Mar	Apr to Sept	Oct to Dec
		Jan to May	Jun to Sept	Oct to Dec
		Jan to Apr	May to Oct	Nov to Dec
Mesic ($0.5 < AI$)	AU-Wom	Wet Jan to May	Dry Jun to Oct	Wet Nov to Dec
		Jan to Apr	May to Oct	Nov to Dec
		Jan to Mar	Apr to Oct	Nov to Dec
		Jan to Mar	Apr to Oct	Nov to Dec
		Dry Jan to Mar	Wet Apr to Oct	Dry Nov to Dec
	AU-Tum	Jan to Mar	Apr to Oct	Nov to Dec

normalized RMSD (RMSD/standard deviation) and correlation between observed and modeled H of 27–60% and 0.78–0.95, respectively. Notable differences in λE errors between wet and dry seasons for arid and semi-arid ecosystems (normalized RMSD 90–100%) were not found, but the error in λE was lower (52%) during the wet season as compared to the dry seasons (75%) in the mesic ecosystems. This further highlights the fact that the high errors in λE for dry seasons in arid semi-arid ecosystems are associated with uncertainties in T_R and SEB closure corrections, respectively.

A3. Statistical Analysis

Total RMSD is the sum of RMSD_S and nonsystematic RMSD (RMSD_U), and according to Willmott (1982) RMSDs should be less than RMSD_U . The proportion of the total RMSD arising from systematic biases is reflected in the quantity $\text{RMSD}_S^2/\text{RMSD}^2$ (Willmott, 1982).

$$\text{RMSD} = \left[\frac{1}{N} \sum_{i=1}^N (P_i - O_i)^2 \right]^{0.5} \quad (\text{A1})$$

$$\text{RRMSD} = 100 \left[\frac{\text{RMSD}}{\bar{O}} \right] \quad (\text{A2})$$

$$\text{MAPD} = \frac{100}{\bar{O}} \left[\frac{1}{N} \sum_{i=1}^N |(P_i - O_i)| \right] \quad (\text{A3})$$

$$\frac{\text{RMSD}_S^2}{\text{RMSD}^2} = 100 \frac{\left[\frac{1}{N} \sum_{i=1}^N (\hat{P}_i - O_i)^2 \right]^{0.5}}{\left[\frac{1}{N} \sum_{i=1}^N (P_i - O_i)^2 \right]^{0.5}} \quad (\text{A4})$$

where O_i represents observed value, P_i is the model-predicted value, N number of observations, \hat{P}_i estimated value based on the ordinary least square regression ($\hat{P}_i = c + mO_i$); where m and c are the slope and intercept of linear regression between P on O , and \bar{O} is the mean of observed values.

Acknowledgments

This study was funded by the Luxembourg Institute of Science and Technology (LIST) under project BIOTRANS (project code 00001145). Partial funding for this research was provided through the FNR-DGF CAOS-2 project grant (INTER/DFG/14/02); and through HiWET (High-resolution modeling and monitoring of Water and Energy Transfers in wetland ecosystems) consortium funded by BELSPO and FNR under the programme STEREOIII (INTER/STEREOIII/13/03/HiWET; contract NR SR/00/301). We are grateful to all Australian and international collaborators, OzFlux PIs, and all the funding agencies that have contributed to establishing Terrestrial Ecosystem Research Network (TERN) and Ozflux. The authors declare no conflict of interest. This work utilized data collected by grants funded by the Australian Research Council (DP0344744, DP0772981, DP120101735, DP130101566, and LE0882936). Jason Beringer is funded under an ARC Future Fellowship (FT110100602). DTD acknowledges support of the Jet Propulsion Laboratory, California Institute of Technology, under a contract with the National Aeronautics and Space Administration. KM designed the analysis; ET and KM performed the analysis; KM, ET, and IT developed the initial version of the manuscript; and all the coauthors make significant contribution in editing the manuscript. The authors declare no conflict of interests. Data used in the current analysis is available through the OzFlux data portal (<http://data.ozflux.org.au/portal/pub/listPubCollections.jsp>), and we have used data level-3 data that was available in csv format in the fluxnet repository (<http://data.ozflux.org.au/portal/pub/viewColDetails.jsp?collection.id=1882723&collection.owner.id=450&viewType=anonymous>).

References

- Abdi, A. M., Boke-Olén, N., Tenenbaum, D. E., Tagesson, T., Cappelaere, B., & Ardö, J. (2017). Evaluating water controls on vegetation growth in the semi-arid Sahel using field and Earth observation data. *Remote Sensing*, 9, 294. <https://doi.org/10.3390/rs9030294>
- Allen, R. G., Pereira, L. S., Raes, D., & Smith, M. (1998). *Crop evapotranspiration: Guidelines for computing crop water requirements* (Irrig. and Drainage Pap. 56). Rome, Italy: Food and Agriculture Organization of the United Nations.
- Anderson, M. C., Allen, R., Morse, A., & Kustas, W. P. (2012). Use of Landsat thermal imagery in monitoring evapotranspiration and managing water resources. *Remote Sensing Environment*, 122, 50–65. <https://doi.org/10.1016/j.rse.2011.08.025>
- Anderson, M. C., Norman, J. M., Kustas, W. P., Houborg, R., Starks, P., & Agam, N. (2008). A thermal-based remote sensing technique for routine mapping of land-surface carbon, water and energy fluxes from field to regional scales. *Remote Sensing of Environment*, 112(12), 4227–4241. <https://doi.org/10.1016/j.rse.2008.07.009>
- Anderson, M. C., Norman, J. M., Mecikalski, J. R., Otkin, J. A., & Kustas, W. P. (2007). A climatological study of evapotranspiration and moisture stress across the continental United States based on thermal remote sensing. 1: Model formulation. *Journal of Geophysical Research*, 112, D10117. <https://doi.org/10.1029/2006JD007506>
- Barr, A. G., van der Kamp, G., Black, T. A., McCaughey, H., & Nesic, Z. (2012). Energy balance closure at the BERMS flux towers in relation to the water balance of the White Gull Creek watershed 1999–2009. *Agricultural and Forest Meteorology*, 153, 3–13. <https://doi.org/10.1016/j.agrformet.2011.05.017>
- Beringer, J., Hutley, L. B., McHugh, I., Arndt, S. K., Campbell, D., Cleugh, H. A., et al. (2016). An introduction to the Australian and New Zealand flux tower network—OzFlux. *Biogeosciences*, 13, 5895–5916. <https://doi.org/10.5194/bg-13-5895-2016>
- Bhattarai, N., Mallick, K., Brunsell, N. A., Sun, G., & Jain, M. (2017). Regional evapotranspiration from image-based implementation of the Surface Temperature Initiated Closure (STIC1.2) model and its validation across an aridity gradient in the conterminous United States. *Hydrology and Earth System Sciences*, 22, 2311–2341. <https://doi.org/10.5194/hess-22-2311-2018>
- Boegh, E., & Soegaard, H. (2004). Remote sensing based estimation of evapotranspiration rates. *International Journal of Remote Sensing*, 25, 2535–2551.
- Boegh, E., Soegaard, H., & Thomsen, A. (2002). Evaluating evapotranspiration rates and surface conditions using Landsat TM to estimate atmospheric resistance and surface resistance. *Remote Sensing Environment*, 79, 329–343.
- Boulet, G., Mougenot, B., Lhomme, J.-P., Fanise, P., Lili-Chabaane, Z., Olioso, A., et al. (2015). The SPARSE model for the prediction of water stress and evapotranspiration components from thermal infra-red data and its evaluation over irrigated and rainfed wheat. *Hydrology and Earth System Sciences*, 19, 4653–4672. <https://doi.org/10.5194/hess-19-4653-2015>
- Boulet, G., Olioso, A., Ceschia, F., Marloie, O., Coudert, B., & Rivalland, A. (2012). An empirical expression to relate aerodynamic and surface temperatures for use within single-source energy balance models. *Agricultural and Forest Meteorology*, 161, 148–155. doi:10.1016/j.agrformet.2012.03.008.
- Bowen, I. (1926). The ratio of heat losses by conduction and by evaporation from any water surface. *Physical Review*, 27(6), 779–787. <https://doi.org/10.1103/PhysRev.27.779>
- Brutsaert, W., & Stricker, H. (1979). An advection-aridity approach to estimate actual regional evapotranspiration. *Water Resources Research*, 15(2), 443–450. <https://doi.org/10.1029/WR015i002p00443>
- Chávez, J. L., Howell, T. A., Gowda, P. H., Copeland, K. S., & Prueger, J. H. (2010). Surface aerodynamic temperature modeling over rainfed cotton. *Transactions of the ASABE*, 53(3), 759–767.
- Chávez, J. L., Neale, C. M. U., Hipps, L. E., Prueger, J. H., & Kustas, W. P. (2005). Comparing aircraft-based remotely sensed energy balance fluxes with eddy covariance tower data using heat flux source area functions. *Journal of Hydrometeorology*, 6, 923–940.
- Cleverly, J., Chen, C., Boulain, N., Villalobos-Vega, R., Faux, R., Grant, N., et al. (2013). Aerodynamic resistance and Penman-Monteith evapotranspiration over a seasonally two-layered canopy in semi-arid central Australia. *Journal of Hydrometeorology*, 14, 1562–1570. <https://doi.org/10.1175/jhm-d-13-080.1>
- Cleverly, J., Eamus, D., Van Gorsel, E., Chen, C., Rumman, R., Luod, Q., et al. (2016). Productivity and evapotranspiration of two contrasting semi-arid ecosystems following the 2011 global carbon land sink anomaly. *Agricultural and Forest Meteorology*, 220, 151–159. <https://doi.org/10.1016/j.agrformet.2016.01.086>
- Colaizzi, P. D., Agam, N., Tolk, J. A., Evett, S. R., Howell, T. A., Gowda, P. H., et al. (2014). Two-source energy balance model to calculate E, T, and ET: Comparison of Priestley-Taylor and Penman-Monteith formulations and two time scaling methods. *Transactions of the ASABE*, 57(2), 479–498. <https://doi.org/10.13031/trans.57.10423>
- Colaizzi, P. D., Evett, S. R., Howell, T. A., & Tolk, J. A. (2004). Comparison of aerodynamic and radiometric surface temperature using precision weighing lysimeters, Remote Sensing and modeling of ecosystems for sustainability. In *Proceedings of SPIE* (Vol. 5544). Bellingham, WA: SPIE. <https://doi.org/10.1117/12.559503>
- Colaizzi, P. D., Kustas, W. P., Anderson, M. C., Agam, N., Tolk, J. A., Evett, S. R., et al. (2012). Two-source energy balance model estimates of evapotranspiration using component and composite surface temperatures. *Advances in Water Research*, 50, 134–151. <https://doi.org/10.1016/j.advwatres.2012.06.004>
- Crago, R. D., & Qualls, R. J. (2014). Use of land surface temperature to estimate surface energy fluxes: Contributions of Wilfried Brutsaert and collaborators. *Water Resources Research*, 50, 3396–3408. <https://doi.org/10.1002/2013WR015223>
- Dirmeyer, P. A. (2011). The terrestrial segment of soil moisture-climate coupling. *Geophysical Research Letters*, 38, L16702. <https://doi.org/10.1029/2011GL048268>
- Donohue, R. J., Roderick, M. L., & McVicar, T. R. (2010). Can dynamic vegetation information improve the accuracy of Budyko's hydrological model? *Journal of Hydrology*, 390, 23–34. <https://doi.org/10.1016/j.jhydrol.2010.06.025>
- Ershadi, A., McCabe, M. F., Evans, J. P., & Wood, E. F. (2015). Impact of model structure and parameterization on Penman-Monteith type evaporation models. *Journal of Hydrology*, 525, 521–535. <https://doi.org/10.1016/j.jhydrol.2015.04.008>
- Foken, T. (2008). The energy balance closure problem: An overview. *Ecological Applications*, 18, 1351–1367. <https://doi.org/10.1890/06-0922.1>
- Formetta, G., Banerji, M., David, O., & Rigon, R. (2016). Performance of site-specific parameterizations of longwave radiation. *Hydrology and Earth System Sciences*, 20, 4641–4654. <https://doi.org/10.5194/hess-20-4641-2016>

- French, A. N., Hunsaker, D. J., & Thorp, K. R. (2015). Remote sensing of evapotranspiration over cotton using the TSEB and METRIC energy balance models. *Remote Sensing Environment*, 158, 281–294. <https://doi.org/10.1016/j.rse.2014.11.003>
- García, M., Oyonarte, C., Villagarcía, L., Contreras, S., Domingo, F., & Puigdefábregas, J. (2008). Monitoring land degradation risk using ASTER data: The non-evaporative fraction as an indicator of ecosystem function. *Remote Sensing Environment*, 112, 3720–3736. <https://doi.org/10.1016/j.rse.2008.05.011>
- Glenn, E., Doody, T. M., Guerschman, J. P., Huete, A. R., King, E. A., McVicar, T. R., et al. (2011). Actual evapotranspiration estimation by ground and remote sensing methods: The Australian experience. *Hydrological Processes*, 25, 4103–4116. <https://doi.org/10.1002/hyp.8391>
- Göttsche, F. M., & Hulley, G. C. (2012). Validation of six satellite-retrieved land surface emissivity products over two land cover types in a hyper-arid region. *Remote Sensing Environment*, 124, 149–158.
- Guerschman, J., Van Dijk, A. I. J. M., Mattersdorf, G., Beringer, J., Hutley, L. B., Leuning, R., et al. (2009). Scaling of potential evapotranspiration with MODIS data reproduces flux observations and catchment water balance observations across Australia. *Journal of Hydrology*, 369, 107–119. <https://doi.org/10.1016/j.jhydrol.2009.02.013>
- Heitman, J. L., Horton, R., Sauer, T. J., Ren, T. S., & Xiao, X. (2010). Latent heat in soil heat flux measurements. *Agricultural and Forest Meteorology*, 150, 1147–1153. <https://doi.org/10.1016/j.agrformet.2010.04.017>
- Hollinger, D. Y., & Richardson, A. (2005). Uncertainty in eddy covariance measurements and its application to physiological models. *Tree Physiology*, 25, 783–885. <https://doi.org/10.1093/treephys/25.7.873>
- Holwerda, F., Bruijnzeel, L. A., Scatenac, F. N., Vugtsa, H. F., & Meesters, A. G. C. A. (2012). Wet canopy evaporation from a Puerto Rican lower montane rain forest: The importance of realistically estimated aerodynamic conductance. *Journal of Hydrology*, 414–415, 1–15. <https://doi.org/10.1016/j.jhydrol.2011.07.033>
- Hulley, G. C., Hook, S. J., Abbott, E., Malakar, N., Islam, T., & Abrams, M. (2015). The ASTER global emissivity dataset (ASTER GED): Mapping Earth's emissivity at 100 meter spatial scale. *Geophysical Research Letters*, 42, 7966–7976. <https://doi.org/10.1002/2015GL065564>
- Hulley, G. C., Hook, S. J., & Baldrige, A. M. (2010). Investigating the effects of soil moisture on thermal infrared land surface temperature and emissivity using satellite retrievals and laboratory measurements. *Remote Sensing Environment*, 114, 1480–1493. <https://doi.org/10.1016/j.rse.2010.02.002>
- Hulley, G. C., Hughes, T., & Hook, S. J. (2012). Quantifying uncertainties in land surface temperature (LST) and emissivity retrievals from ASTER and MODIS thermal infrared data. *Journal of Geophysical Research*, 117, D23113. <https://doi.org/10.1029/2012JD018506>
- Jackson, R. D., Idso, S. B., Reginato, R. J., & Pinter, P. J. (1981). Canopy temperature as a crop water stress indicator. *Water Resources Research*, 17, 1133–1138. <https://doi.org/10.1029/WR017i004p01133>
- Jarvis, P. G., & McNaughton, K. G. (1986). Stomatal control of transpiration: Scaling up from leaf to region. *Advances in Ecological Research*, 15, 1–49. [https://doi.org/10.1016/S0065-2504\(08\)60119-1](https://doi.org/10.1016/S0065-2504(08)60119-1)
- Jolliffe, I. T. (2002). *Principal component analysis, Series: Springer series in statistics* (2nd ed., Vol. XXIX, 487 p., 28 illus). New York, NY: Springer. ISBN: 978-0-387-95442-4.
- Katul, G., Goltz, S., Hsieh, C. I., Cheng, Y., Mowry, F., & Sigmon, J. (1995). Estimation of surface heat and momentum fluxes using the flux-variance method above uniform and non-uniform terrain. *Boundary-Layer Meteorol.*, 74, 237–260. <https://doi.org/10.1007/BF00712120>
- Koster, R. D., Salvucci, G. D., Rigden, A. J., Jung, M., Collatz, G. J., & Schubert, S. D. (2015). The pattern across the continental United States of evapotranspiration variability associated with water availability. *Frontiers in Earth Science*, 3, 35. <https://doi.org/10.3389/feart.2015.00035>
- Kustas, W. P., & Anderson, M. C. (2009). Advances in thermal infrared remote sensing for land surface modeling. *Agricultural and Forest Meteorology*, 149, 2071–2081. <https://doi.org/10.1016/j.agrformet.2009.05.016>
- Kustas, W. P., Nieto, H., Morillas, L., Anderson, M. C., Alfieri, J. G., Hipps, L. E., et al. (2016). Revisiting the paper “Using radiometric surface temperature for surface energy flux estimation in Mediterranean drylands from a two-source perspective. *Remote Sensing Environment*, 184, 645–653. <https://doi.org/10.1016/j.rse.2016.07.024>
- Leuning, R., Zhang, Y., Rajaud, A., Cleugh, H., & Tu, K. (2008). A simple surface conductance model to estimate regional evaporation using MODIS leaf area index and the Penman-Monteith equation. *Water Resources Research*, 44, W10419. <https://doi.org/10.1029/2007WR006562>
- Li, J., Li, J., Weisz, E., & Zhou, D. K. (2007). Physical retrieval of surface emissivity spectrum from hyperspectral infrared radiances. *Geophysical Research Letters*, 34, L16812. <https://doi.org/10.1029/2007GL030543>
- Liu, S., Lu, L., Mao, D., & Jia, L. (2007). Evaluating parameterizations of aerodynamic resistance to heat transfer using field measurements. *Hydrology and Earth System Sciences*, 11, 769–783. <https://doi.org/10.5194/hess-11-769-2007>
- Ma, X., Huete, A., Cleverly, J., Eamus, D., Chevallier, F., Joiner, J., et al. (2016). Drought rapidly diminishes the large net CO₂ uptake in 2011 over semi-arid Australia. *Scientific Reports*, 6, 37747. <https://doi.org/10.1038/srep37747>
- Majazi, N. P., Mannaerts, C. M., Ramoelo, A., Mathieu, R., Nickless, A., & Verhoef, W. (2017). Analysing surface energy balance closure and partitioning over a semi-arid savanna FLUXNET site in Skukuza, Kruger National Park, South Africa. *Hydrology and Earth System Sciences*, 21, 3401–3415. <https://doi.org/10.5194/hess-21-3401-2017>
- Mallick, K., Boegh, E., Trebs, I., Alfieri, J. G., Kustas, W. P., Prueger, J. H., et al. (2015). Reintroducing radiometric surface temperature into the Penman-Monteith formulation. *Water Resources Research*, 51, 6214–6243. <https://doi.org/10.1002/2014WR016106>
- Mallick, K., Jarvis, A. J., Boegh, E., Fisher, J. B., Drewry, D. T., Tu, K. P., et al. (2014a). A surface temperature initiated closure (STIC) for surface energy balance fluxes. *Remote Sensing Environment*, 141, 243–261. <https://doi.org/10.1016/j.rse.2013.10.022>
- Mallick, K., Jarvis, A. J., Wohlfahrt, G., Kiely, G., Hirano, T., Miyata, A., et al. (2014b). Components of near-surface energy balance derived from satellite soundings—Part 2: Noontime latent heat flux. *Biogeosciences*, 11, 7369–7382. <https://doi.org/10.5194/bg-11-7369-2014>
- Mallick, K., Trebs, I., Boegh, E., Giustarini, L., Schlerf, M., Drewry, D. T., et al. (2016). Canopy-scale biophysical controls of transpiration and evaporation in the Amazon Basin. *Hydrology and Earth System Sciences*, 20, 4237–4264. <https://doi.org/10.5194/hess-20-4237-2016>
- Martens, B., Miralles, D., Lievens, H., Fernandez-Prieto, D., & Verhoest, N. (2016). Improving terrestrial evaporation estimates over continental Australia through assimilation of SMOS soil moisture. *International Journal of Applied Earth Observation and Geoinformation*, 48, 146–162. <https://doi.org/10.1016/j.jag.2015.09.012>
- Masiello, G., Serio, C., Venafrà, S., DeFeis, I., & Borbas, E. E. (2014). Diurnal variation in Sahara desert sand emissivity during the dry season from IASI observations. *Journal of Geophysical Research: Atmospheres*, 119, 1626–1638. <https://doi.org/10.1002/jgrd.50863>
- Masseroni, D., Corbari, C., & Mancini, M. (2014). Limitations and improvements of the energy balance closure with reference to experimental data measured over a maize field. *Atmósfera*, 27, 335–352. [https://doi.org/10.1016/S0187-6236\(14\)70033-5](https://doi.org/10.1016/S0187-6236(14)70033-5)
- McHugh, T. A., Morrissey, E. M., Reed, S. C., Hungate, B. A., & Schwartz, E. (2015). Water from air: An overlooked source of moisture in arid and semi-arid regions. *Scientific Report*, 5, 13767. <https://doi.org/10.1038/srep13767>
- Mira, M., Valor, E., Boluda, R., Caselles, V., & Coll, C. (2007). Influence of soil water content on the thermal infrared emissivity of bare soils: Implication for land surface temperature determination. *Journal of Geophysical Research*, 112, F04003. <https://doi.org/10.1029/2007JF000749>

- Monteith, J. L. (1965). Evaporation and environment. In G. E. Fogg (Ed.) *Symposium of the society for experimental biology. The state and movement of water in living organisms* (Vol. 19, pp. 205–234). New York, NY: Academic Press, Inc.
- Monteith, J. L. (1981). Evaporation and surface temperature. *Quarterly Journal of the Royal Meteorological Society*, 107, 1–27. <https://doi.org/10.1002/qj.49710745102>
- Monteith, J. L. (1995). Accommodation between transpiring vegetation and the convective boundary layer. *Journal of Hydrology*, 166, 251–263. [https://doi.org/10.1016/0022-1694\(94\)05086-D](https://doi.org/10.1016/0022-1694(94)05086-D)
- Morillas, L., García, M., Nieto, H., Villagarcía, L., Sandholt, I., Gonzalez-Dugo, M., et al. (2013). Using radiometric surface temperature for energy flux estimation in Mediterranean drylands from a two-source perspective. *Remote Sensing Environment*, 136, 234–246. <https://doi.org/10.1016/j.rse.2013.05.010>
- Norman, J. M., Kustas, W. P., & Humes, K. S. (1995). Source approach for estimating soil and vegetation energy fluxes in observations of directional radiometric surface temperature. *Agricultural and Forest Meteorology*, 77, 263–293. [https://doi.org/10.1016/0168-1923\(95\)02265-Y](https://doi.org/10.1016/0168-1923(95)02265-Y)
- Ochsner, T. E., Sauer, T. J., & Horton, R. (2006). Field tests of the soil heat flux plate method and some alternatives. *Agronomy Journal*, 98, 1005–1014. <https://doi.org/10.2134/agronj2005.0249>
- Park, G.-H., Gao, X., & Sorooshian, S. (2008). Estimation of surface longwave radiation components from ground-based historical net radiation and weather data. *Journal of Geophysical Research*, 113, D04207. <https://doi.org/10.1029/2007JD008903>
- Paul, G., Gowda, P., Varaprasad, P., Howell, T. A., Aiken, R., & Neale, C. (2014). Investigating the influence of roughness length for heat transport (zoh) on the performance of SEBAL in semi-arid irrigated and dryland agricultural systems. *Journal of Hydrology*, 509, 231–234. <https://doi.org/10.1016/j.jhydrol.2013.11.040>
- Paul, G., Gowda, P. H., Vara Prasad, P. V., Howell, T. A., & Staggenborg, S. A. (2013). Lysimetric evaluation of SEBAL using high resolution airborne imagery from BEAREX08. *Advances in Water Research*, 59, 157–168. <https://doi.org/10.1016/j.advwatres.2013.06.003>
- Perez, P. J., Castellvi, F., Ibanez, M., & Rosell, J. I. (1999). Assessment of reliability of Bowen ratio method for partitioning fluxes. *Agricultural and Forest Meteorology*, 97, 141–150. [https://doi.org/10.1016/S0168-1923\(99\)00080-5](https://doi.org/10.1016/S0168-1923(99)00080-5)
- Priestley, C. H. B., & Taylor, R. J. (1972). On the assessment of surface heat flux and evaporation using large scale parameters. *Monthly Weather Review*, 100, 81–92. [https://doi.org/10.1175/1520-0493\(1972\)100<0081:OTAOSH>2.3.CO;2](https://doi.org/10.1175/1520-0493(1972)100<0081:OTAOSH>2.3.CO;2)
- Raupach, M. R. (1998). Influence of local feedbacks on land-air exchanges of energy and carbon. *Global Change Biology*, 4, 477–494. <https://doi.org/10.1046/j.1365-2486.1998.t01-1-00155.x>
- Saadi, S., Boulet, G., Bahir, M., Brut, A., Delogu, E., Fanise, P., et al. (2017). Assessment of actual evapotranspiration over a semi-arid heterogeneous land surface by means of coupled low resolution remote sensing data with energy balance model: Comparison to extra Large Aperture Scintillometer measurements. *Hydrology and Earth System Sciences Discussions*, 22, 2187–2209. <https://doi.org/10.5194/hess-2017-454>
- Shuttleworth, W. J., Gurney, R. J., Hsu, A. Y., & Ormsby, J. P. (1989). FIFE: The variation in energy partition at surface flux sites. In A. Rango (Ed.), *Remote sensing and large scale processes, Proceedings of the IAHS Third International Assembly* (Vol. 186, pp. 67–74). Baltimore, MD, IAHS Publ.
- Shuttleworth, W. J., & Wallace, J. (1985). Evaporation from sparse crops—an energy combination theory. *Quarterly Journal of the Royal Meteorological Society*, 111, 839–855. <https://doi.org/10.1002/qj.49711146910>
- Siqueira, M., Katul, G., & Porporato, A. (2008). Onset of water stress, hysteresis in plant conductance, and hydraulic lift: Scaling soil water dynamics from millimeters to meters. *Water Resources Research*, 44, W01432. <https://doi.org/10.1029/2007WR006094>
- Song, L., Kustas, W. P., Liu, S., Colaizzi, P. D., Nieto, H., Xu, Z., et al. (2016). Applications of a thermal-based two-source energy balance model using Priestley-Taylor approach for surface temperature partitioning under advective conditions. *Journal of Hydrology*, 540, 574–587. <https://doi.org/10.1016/j.jhydrol.2016.06.034>
- Su, Z. (2002). The surface energy balance system (SEBS) for estimation of turbulent heat fluxes. *Hydrology and Earth System Sciences*, 61, 85–99. <https://doi.org/10.5194/hess-6-85-2002>
- Sun, D., & Pinker, R. T. (2003). Estimation of land surface temperature from a Geostationary Operational Environmental Satellite (GOES-8). *Journal of Geophysical Research*, 108 (D11), 4326. <https://doi.org/10.1029/2002JD002422>
- Timmermans, J., Su, Z., van der Tol, C., Verhoef, A., & Verhoef, W. (2013). Quantifying the uncertainty in estimates of surface–atmosphere fluxes through joint evaluation of the SEBS and SCOPE models. *Hydrology and Earth System Sciences*, 17, 1561–1573. <https://doi.org/10.5194/hess-17-1561-2013>
- Troufleau, D., Lhomme, J. P., Monteny, B., & Vidal, A. (1997). Sensible heat flux and radiometric surface temperature over sparse Sahelian vegetation. I: An experimental analysis of kB-1 parameter. *Journal of Hydrology*, 188–189, 815–838. [https://doi.org/10.1016/S0022-1694\(96\)03172-1](https://doi.org/10.1016/S0022-1694(96)03172-1)
- van Dijk, A. I. J. M., Beck, H. E., Crosbie, R. S., de Jeu, R. A. M., Liu, Y. Y., Podger, G. M., et al. (2013). The Millennium Drought in southeast Australia (2001–2009): Natural and human causes and implications for water resources, ecosystems, economy, and society. *Water Resources Research*, 49, 1040–1057. <https://doi.org/10.1002/wrcr.20123>
- van Dijk, A. I. J. M., Gash, J. H., van Gorsel, E., Blanken, P. D., Cescatti, A., Emmel, C., et al. (2015). Rainfall interception and the coupled surface water and energy balance. *Agricultural and Forest Meteorology*, 214–215, 402–415. <https://doi.org/10.1016/j.agrformet.2015.09.006>
- Venturini, V., Islam, S., & Rodriguez, L. (2008). Estimation of evaporative fraction and evapotranspiration from MODIS products using a complementary based model. *Remote Sensing Environment*, 112, 132–141. <https://doi.org/10.1016/j.rse.2007.04.014>
- Wang, J., Zhuang, J., Wang, W., Liu, S., & Xu, Z. (2015). Assessment of uncertainty in eddy covariance flux measurement based on intensive flux matrix of HiWATER-MUSOEXE. *IEEE Geoscience and Remote Sensing Letters*, 12 (2), 259–264. <https://doi.org/10.1109/LGRS.2014.2334703>
- Willmott, C. J. (1982). Some comments on the evaluation of model performance. *Bulletin of the American Meteorological Society*, 63, 1309–1313. [https://doi.org/10.1175/1520-0477\(1982\)063<1309:SCOTEO>2.0.CO;2](https://doi.org/10.1175/1520-0477(1982)063<1309:SCOTEO>2.0.CO;2)
- Winter, J. M., & Eltahir, E. A. B. (2010). The sensitivity of latent heat flux to changes in the radiative forcing: A framework for comparing models and observations. *Journal of Climate*, 23, 2345–2356. <https://doi.org/10.1175/2009JCLI3158.1>
- Zhang, Q., Manzoni, S., Katul, G., Porporato, A., & Yang, D. (2014). The hysteretic evapotranspiration—Vapor pressure deficit relation. *Journal of Geophysical Research: Biogeosciences*, 119, 125–140. <https://doi.org/10.1002/2013JG002484>